

Computational modelling of blood flow through sutured and coupled microvascular anastomoses

by

Richard A J Wain

A thesis submitted in partial fulfilment for the requirements for the degree of
MSc (by Research) at the University of Central Lancashire

April 2013

Student Declaration

Concurrent registration for two or more academic awards

Either *I declare that while registered as a candidate for the research degree, I have not been a registered candidate or enrolled student for another award of the University or other academic or professional institution

or ~~*I declare that while registered for the research degree, I was with the University's specific permission, a *registered candidate/*enrolled student for the following award:~~

Material submitted for another award

Either *I declare that no material contained in the thesis has been used in any other submission for an academic award and is solely my own work

or ~~*I declare that the following material contained in the thesis formed part of a submission for the award of~~

(state award and awarding body and list the material below):

** delete as appropriate*

Collaboration

Where a candidate's research programme is part of a collaborative project, the thesis must indicate in addition clearly the candidate's individual contribution and the extent of the collaboration. Please state below:

N/A



Signature of Candidate

Type of Award**Master of Science by Research**.....

School ..**School of Computing, Engineering & Physical Sciences**..

Declaration

No part of the work described in this thesis has been submitted to this University or any other establishment of learning for this, or any other, award.

Abstract

The research presented in this thesis uses Computational Fluid Dynamics (CFD) to model blood flow through idealised sutured and coupled microvascular anastomoses to investigate the affect of each surgical technique on the flow within the vessel. Local flow phenomena are examined in detail around suture and coupler sites to study characteristics that could potentially initiate thrombus formation; for example, changes in velocity profile, wall shear stress or recirculating flow (vorticity).

Idealised geometries of sutured and coupled blood vessels were created using CFD software with dimensions identical to microvascular suture material and coupling devices. Vessels were modelled as non-compliant 1 mm diameter ducts, and blood was simulated as a Newtonian fluid, in keeping with previous similar studies. All analyses were steady-state and performed on arteries.

Comparison of the sutured and coupled techniques in the simulated microarterial anastomoses revealed a reduced boundary velocity profile; high Wall Shear Stress (WSS); high Shear Strain Rate (SSR); and elevated vorticity at the suture sites. The coupled anastomosis simulation showed a small increase in maximum WSS at the anastomotic region compared to a pristine vessel. However, this was less than half that of the sutured model. The coupled vessel displayed an average WSS equal to a pristine vessel.

Taken together, these observations demonstrate an increased thrombogenic profile in the sutured anastomosis when compared to a pristine, or indeed a coupled vessel. Data from the simulations on a coupled anastomosis reveal a profile that is less thrombogenic than that of the sutured anastomosis, and one that is nearly equivalent to that of a pristine vessel.

Overall, it can be concluded that, within the limits of CFD simulations and the assumptions taken in this study, a sutured anastomosis is potentially more likely to generate an intravascular thrombosis than a coupled anastomosis.

Contents

Declaration	ii
Abstract	iii
Acknowledgements	viii
Abbreviations.....	ix
1 Introduction	1
1.1 Background of microsurgery and free tissue transfer.....	1
1.2 Rationale for this research	2
1.3 Fluid dynamics.....	3
1.3.1 Concept of a fluid	3
1.4 Aim and objectives	6
1.4.1 Aim	6
1.4.2 Working hypothesis.....	6
1.4.3 Objectives.....	6
1.5 Overview of the thesis	7
2 Background	8
2.1 Anastomotic techniques	8
2.1.1 Current practices.....	9
2.2 Fluid dynamics.....	13
2.2.1 Control volume analysis	13
2.2.2 Differential analysis.....	15
2.2.3 Dimensional analysis	18
2.3 CFD	18
2.3.1 Fundamentals.....	19
2.3.2 CFD and blood flow modelling	20
2.3.3 CFD software codes.....	24
2.4 Boundary conditions and material properties	26
2.5 Flow effects and blood coagulation	28
2.6 Introduction of methods.....	29
3 Methods.....	31
3.1 Vessel fluid geometry creation.....	31
3.1.1 Pristine model	31
3.1.2 Sutured anastomosis.....	32
3.1.3 Coupled anastomosis	32
3.2 Meshing techniques	37

3.3	Boundary conditions	39
3.3.1	Inlet	39
3.3.2	Outlet	46
3.3.3	Wall	46
3.3.4	Symmetry	46
3.4	Post-processing	46
3.5	Statistical analysis	48
4	Results	49
4.1	Vessel simulations	49
4.1.1	Velocity profiles	50
4.1.2	Pressure contours	54
4.1.3	Wall Shear Stress (WSS) and Shear Strain Rate (SSR)	60
4.1.4	Vorticity	66
4.2	Statistical analysis	68
5	Discussion	70
5.1	Clinical	70
5.2	Analytical	72
5.3	Summary	73
6	Conclusions and recommendations	76
6.1	Conclusions	76
6.2	Recommendations for further work	77
	References	79
	Presentations and publications	86

List of Figures

Figure 2.1 - Demonstrating a sutured anastomosis being performed under an operating microscope	10
Figure 2.2 - (a) A 4.0 mm coupler in winged-jaw assembly anastomotic device, with one ring turned perpendicular to the vessel at the left that will be first attached, (b) vein initially impaled over pins at opposite ends of the major axis of the ring, (c) next, vein is everted over the pins opposite the minor axis at the ring midpoint, (d) completed fixation of vein onto all pins, (e) finished anastomosis (<i>adapted from (28)</i>).....	11
Figure 2.3 – Illustrating the cylindrical coordinates (from (39))	17
Figure 3.1 - Suture three-dimensional modelling process (a) tori ring (b) subtraction body operation	32
Figure 3.2 - CATIA coupled anastomosis (a) assembly (b) exploded assembly.....	33
Figure 3.3 - CATIA anastomosis assembly parts (a) coupler flange, (b) pin and (c) vessel section	33
Figure 3.4 - Micrographs of coupling device (a) plan and (b) side elevation used to construct CATIA model	34
Figure 3.5 - CATIA coupler sub-assembly.....	35
Figure 3.6 - Control volume creation (a) section creation, (b) resulting section and (c) symmetric fluid volume	36
Figure 3.7 - Meshes of the anastomotic region in the sutured (a) & (b) and coupled (c) & (d) models	39
Figure 3.8 - ANSYS-CFX (a) pristine, (b) sutured and (c) coupled blood vessel models, inc. boundary conditions.....	40
Figure 3.9 - Paraboloid velocity distribution in a straight rigid circular vessel with constant flow (created in MathWorks MATLAB).....	41
Figure 3.10 - Comparison of theoretical and analytical velocity profiles.....	42
Figure 4.1 - Pristine CFX streamlines (a) velocity profile, (b) boundary layer velocity profile	51
Figure 4.2 - Sutured CFX streamlines (a) velocity profile, (b) boundary layer velocity profile and (c) close up of single suture boundary layer velocity profile with underlying mesh	52
Figure 4.3 - Coupled CFX streamlines (a) velocity profile, (b) internal boundary layer velocity profile	54
(a) (b) Figure 4.4 - Pristine CFX pressure contours at (a) symmetry plane and (b) wall	56
Figure 4.5 - Pristine CFD and theoretical pressure profile comparisons.....	57
Figure 4.6 - Sutured CFX pressure contours at (a) symmetry plane and (b) wall	58
Figure 4.7 - Coupled CFX pressure contours at (a) symmetry plane and (b) wall.....	59
Figure 4.8 - Pristine CFX wall shear stress contour	61
Figure 4.9 - Sutured CFX wall shear stress contour at (a) whole vessel, (b) anastomosis and (c) close up of single suture	62
Figure 4.10 - Sutured CFX shear strain rate at the anastomosis site	63
Figure 4.11 - Coupled CFX wall shear stress contour at (a) whole vessel and (b) close up of coupler site	64
Figure 4.12 - Coupled CFX shear strain rate at the anastomosis site	65
Figure 4.13 - Vorticity profiles for (a) sutured and (b) coupled simulations.....	67

List of Tables

Table 3.1 - Mesh reports for vessel geometries	37
Table 4.1 - Summary of input data parameters	49
Table 4.2 - Mean and maximum boundary velocity comparison inc. SEM depicted as ANSYS default of 10%.....	53
Table 4.3 - Mean and maximum wall shear stress comparison inc. SEM depicted as ANSYS default of 10%.....	64
Table 4.1 - Student's t-test of WSS for sutured and coupled simulations ($p < 0.1\%$)	69
Table 5.1 - F test (Fisher's) for WSS in sutured and coupled simulations ($p < 2\%$).....	72

Acknowledgements

Thanks to my supervisory team: Dr Justin Whitty, Prof. Mike Holmes, Prof. Waqar Ahmed and Mr Milind Dalal for their advice, direction and motivation. In particular, Dr Whitty has sacrificed a significant portion of his personal time to assist me with the more complex aspects of the research and, without his enthusiasm and attention to rigor; the project would not have been such a success.

Thanks to the Rosemere Cancer Foundation for their financial support and to NorthStar for supply of the microvascular coupling devices.

Thanks to my ever-supportive wife, Alex, for everything she has done to help me complete this period of research. I could not have done it without her.

I dedicate this thesis to my newly born daughter, Evie Catherine Rose.



Abbreviations

CABG – Coronary Artery Bypass Graft

CAD – Computer Aided Design

CATIA – Computer Aided Interactive Three-dimensional Application

ceMRI – Contrast enhanced Magnetic Resonance Imaging

CFD – Computational Fluid Dynamics

CT – Computed Tomography

FEM – Finite Element Model

FGF-2 – Fibroblast Growth Factor-2

IMA – Internal Mammary Artery

MAC – Microvascular Anastomotic Coupling

MRI – Magnetic Resonance Imaging

NICE – National Institute for Health and Clinical Excellence

PDE – Partial Differential Equations

SEM – Standard Error of the Mean

SSR – Shear Strain Rate

UK – United Kingdom

USA – United States of America

VCS – Vascular Clip System

WSS – Wall Shear Stress

1 Introduction

This chapter provides an overview of microsurgery and its applications within reconstructive surgery, along with a synopsis of fluid dynamics and Computational Fluid Dynamics (CFD). The rationale for this research is also given, and the aim and objectives of the thesis stated.

1.1 Background of microsurgery and free tissue transfer

Microsurgery is defined as a group of surgical procedures performed with the aid of magnification that would otherwise be impossible with the naked eye. The origins of microvascular surgery date back to the late nineteenth and early twentieth century, with the first successful end-to-end anastomosis being performed by Jassinowski (1) using fine silk sutures. The Nobel Prize-winning work of Carrel (2) has led to the standardised triangulation method of placing microvascular sutures.

The next fifty years saw significant developments in fine instruments, magnification, pharmaceuticals such as heparin, and refinement of microsurgical technique. In 1960 Jacobson performed the first 'microvascular anastomosis' in carotid arteries of laboratory animals as small as 1.4 mm diameter, achieving a 100% patency rate (3).

Once a reliable technique for microvascular anastomosis was established, its use became more widespread. Successful replantations of firstly upper limbs (4), then digits (5) were performed, and by the early 1970s free tissue transfer was reported by several different centres (6–8).

Since the 1970s, the work carried out by these early pioneers has been refined to provide reconstructive options for the entire body and, more recently, allotransplantation of complex anatomical units including whole hands and faces (9).

Free tissue transfer involves removing tissue from one place on a patient's body, along with its main blood vessels, positioning it over a defect, and anastomosing the blood vessels to existing vessels in the region of the defect. Numerous indications exist for free tissue transfer and hence, microvascular anastomosis within plastic and reconstructive surgery. The key factor influencing need for free tissue is the nature of the defect it is intended to reconstruct (10). Consideration must be given to the tissue characteristics such as size, colour, and composition (e.g. skin, fascia, muscle, bone, and nerve), aesthetics, length of pedicle, and vessel matching (11).

Specific indications for free tissue transfer reconstruction include:¹

- Obliteration of dead space e.g. after extensive soft tissue resection
- Coverage of exposed bone/neurovascular tissue e.g. lower limb trauma
- Restoration of volume and contour e.g. post-mastectomy breast
- Insetting of vascularised enteral conduit e.g. following pharyngeal resection
- Reconstruction of composite defects e.g. floor of mouth and mandible
- Replacement of functional muscle e.g. facial reanimation
- Revascularisation/replantation of appendages e.g. digits/limb

1.2 Rationale for this research

Breast cancer affects over 40, 000 people per year in the UK and is now the country's most common cancer (12). Head and neck cancers affect approximately 5, 000 people per year in the UK.

¹ Adapted from Table 8.1 from (11)

The majority of these patients will require some form of surgical procedure as part of their definitive management. Approximately 40% of breast cancer patients will undergo a mastectomy (12) and, as per the National Institute for Health and Clinical Excellence (NICE) guidelines, all should be offered the chance of breast reconstruction, which can either be immediate or delayed. Although many different reconstructive options exist, there are a significant number of patients who undergo reconstruction using free tissue transfer.

In the early postoperative period, the viability of the free flap depends largely on the arterial supply and venous drainage of the anastomosed vessels. The incidence of free flap failure is approximately 5% (13), with the majority of these due to a clot in one of the vessels. Blood clots have a propensity to form within vessels when there is an alteration in the blood composition, the vessel wall, or the local blood flow (14).

The consequences of a failed anastomosis can be catastrophic for the patient from both a physical and psychological viewpoint. In the short term, it can lead to further surgery, a longer hospital stay and its associated risks, and potentially systemic infection. In the long term, it can cause uneven and disfiguring body contours.

1.3 Fluid dynamics

In order to successfully and accurately model blood flow in microvascular anastomoses, it is essential to consider the fundamental properties and behaviour of fluids in general.

1.3.1 Concept of a fluid

A fluid is defined as a substance that deforms when a shear stress, no matter how small, is applied to it. The fluid will move continuously under the influence of the shear stress for as long as it is applied, and it is therefore also possible to say that a fluid at rest must be in a state of zero shear stress (15,16).

There are two principal methods of describing the analysis of fluid flows. First is the *Eulerian* method. This is concerned with addressing the field of flow, and describes the flow field as functions of space coordinates and time. It is the most commonly used approach and forms the basis of the analyses in this research. The second method is the *Lagrangian* approach. This describes the flow by calculating the path of an individual particle flowing through the field (15,16). The Lagrangian approach is often used to describe particulate motion within solid mechanics rather than in fluid mechanical problems.

Apart from in a series of special circumstances, fluids under normal conditions are considered a continuum. This assumes that each fluid property has a definite value at every point in space. As such, properties including velocity and density are considered to be continuous functions of time and position (16). There is a limiting volume however, above which aggregate variations may be important, and below which molecular variations may also be significant. In the vast majority of circumstances, physical dimensions are much larger than this limiting volume and the fluid properties can be considered as varying continually in space i.e. a continuum (15).

It is important to define some of the basic properties of a fluid in order to understand and appreciate the remainder of this section and also to interpret the results presented later in the thesis.

Probably the foremost property of fluid flow is the velocity field $\mathbf{v}(x, y, z, t)$ (15). Velocity is generally considered a vector function of position and time and as such requires a magnitude and direction for a complete description. $\mathbf{v}(x, y, z, t)$ indicates the velocity of a fluid particle at a defined point x, y, z at a time of t . Importantly, x, y and z are independent variables and *do not* represent the on-going position of an individual particle (17). The velocity field interacts closely with other fluid properties including pressure p , density ρ , and viscosity μ .

Pressure p is the compression stress at a point within a static fluid (15). Gradients in pressure along ducts, such as blood vessels in this research, drive the fluid through the duct. In fluid mechanics, pressure is commonly expressed in Pascals (Pa).

The density ρ of a fluid is its mass per unit volume, and in most liquids is nearly constant. Thus, most liquids are considered *incompressible* for analytical purposes (15). Water has a density of approximately $1,000 \text{ kg m}^{-3}$ and blood is slightly denser at approximately $1,060 \text{ kg m}^{-3}$. Further details about the density figures used in this research are given in section 2.4.

Viscosity μ is considered a secondary variable used to describe fluid behaviour. It is a measure of a fluid's resistance to flow in that it determines the Shear Strain Rate (SSR) that is generated by a given shear stress (15). Fluids in which the shear stress is directly proportional to the SSR, or rate of deformation, are said to be *Newtonian* fluids (18). Fluids where the relationship is non-linear are described as *non-Newtonian* (17). Most common fluids such as water and air are Newtonian, and in this research blood will also be considered a Newtonian fluid. Evidence for this is given in detail in section 2.4.

The viscous behaviour of all Newtonian fluids can be estimated using the dimensionless *Reynolds number* (Re), which can be calculated using the expression below (1.1).

$$Re = \rho \frac{vL}{\mu} \tag{1.1}$$

Where ρ and μ are the fluid density and viscosity, respectively; and v and L are the typical velocity magnitude and diameter values, respectively (17). Fluids with a 'low' Reynolds number are said to be viscous dominant and as such exhibit smoothly varying *laminar* flow, whereas fluids with a 'high' Reynolds number typically demonstrate *turbulent* flow. The transition from laminar to turbulent flow depends on many elements such as wall roughness or changes in the inlet stream, but the primary factor is the Reynolds number (19). Although Reynolds number

ranges may vary slightly, White (19), in his text on Fluid Mechanics, proposes approximate values at which flow changes from laminar to turbulent. He states that at Reynolds numbers of less than 1, 000, flow is broadly laminar; between 1, 000 and 10, 000 there is a transition to turbulence, and above 10, 000 flow is certainly turbulent. Importantly, when specifically considering flow in ducts, Reynolds numbers of greater than 2, 300 would render turbulent flow (19). The Reynolds number calculated for the vessels in this research is approximately 90 ($Re \approx 90$), and as such is comfortably within the laminar range.

1.4 Aim and objectives

The aim of the thesis is stated below along with the working hypothesis of the study. A list of objectives is subsequently provided to detail the way in which the aim will be achieved.

1.4.1 Aim

This thesis aims to describe the use of Computational Fluid Dynamics (CFD) to model blood flow characteristics through sutured and coupled microvascular anastomoses, in order to detect flow patterns that may predispose to thrombus formation. Qualitative and quantitative results will be presented to demonstrate the following research hypothesis.

1.4.2 Working hypothesis

Couplers have demonstrated at least equivalent thrombosis rates to those of sutures in venous microanastomoses. The working hypothesis of this study is that arterial coupling may follow a similar pattern, based on the flow properties of each anastomotic technique.

1.4.3 Objectives

In order to fulfil this aim, the following objectives have been identified:

- To identify pertinent empirical and/or analytical/numerical blood rheology data from current literature for entry into suitable CFD software.

- To produce analytical and numerical (CFD) models of idealised Newtonian fluids through a standardised circular duct.
- To utilise computational models in order to mimic the human blood vessel geometries in pristine forms.
- To perform steady-state analyses of microvascular anastomoses using CFD (i.e. through sutured and coupled vessels).
- To correlate modelling data with realistic empirical data evident in the literature, analyse the data and present it in a thesis.

1.5 Overview of the thesis

Chapter 2 details the applicable literature including current anastomotic techniques and previous work investigating computational modelling of flow in blood vessels. It should be noted that a thorough examination of the existing literature has revealed no studies that have evaluated CFD of flow through microvascular coupling devices.

In chapter 3, the modelling methods are discussed. This encompasses geometry creation, meshing techniques, application of boundary conditions, post-processing and validation processes.

Chapter 4 focuses on the results obtained during this research. Comprehensive results of the vascular models are given along with their statistical analysis.

The penultimate chapter encompasses discussion of the findings from both a clinical and analytical viewpoint; while in the final chapter, detailed conclusions are drawn from the work presented, and recommendations suggested for further work.

2 Background

2.1 Anastomotic techniques

Historically, vessels have been anastomosed end-to-end using sutures², which remains the preferred method. However, more recently (20) coupling devices have been developed to produce a sutureless anastomosis in the vessels. These coupling devices consist of two polyethylene rings with stainless steel pins that interlock to provide intima-intima³ contact. Couplers have been used in the joining of vessels for several years with venous thrombosis and flap salvage rates approximately equivalent to sutured anastomoses (21). They have mainly been used in venous anastomoses and, according to the literature reviewed here, there are no centres in the UK using them to perform arterial anastomoses, as they are primarily designed for veins.

As well as a thorough review of the PubMed and Medilne databases, a consensus opinion was sought at a meeting of leading UK and international plastic surgeons regarding the use of the coupler in arterial anastomoses. Synovis, the manufacturer of the coupling device, held this meeting in October 2010 where there was widespread agreement that the coupler is not used for arterial anastomosis in the UK. The main reasons for avoiding arterial coupling with this device are the technical difficulties encountered when placing the vessel onto the ring-pins due to the thicker and less pliable walls found in arteries. Further details on the use of the coupler in both arteries and veins are given in section 2.1.1.

There are no current devices specifically designed for arterial coupling however, with the average time taken to complete a hand sutured end-to-end arterial anastomosis being 22.3 minutes (22), and venous coupling devices taking approximately 5 minutes (23) to apply, there

² Material used to close a wound or sew tissues together.

³ The inner layer of blood vessel walls, composed of endothelial cells and an elastic membrane.

is huge potential to reduce arterial ischaemic time with the development of an arterial coupler.

2.1.1 Current practices

The surgical anastomosis of small calibre (2 mm) vessels was originally pioneered by Jacobson & Suarez in 1960 when using fine 7/0⁴ silk sutures to join carotid arteries in dogs (3). Since then significant developments have been made in anastomotic technique, surgical instruments and suture materials in order to try and perform the *ideal* anastomosis. Small calibre vessels are now routinely anastomosed using fine synthetic monofilament⁵ suture with the aid of an operating microscope. This is the current standard, however other techniques have been proposed to form a sutureless anastomosis in order to reduce vessel thrombosis and flap failure rates. Both the Vascular Clip System (VCS) (24) and the Unilink microvascular coupler (20) are such devices, and have been used and accepted as alternatives to suturing to varying extents by the surgical community. Neither method, however, is routine practice in many units because of cost implications, operator experience and surgeon preference.

Sutured

Microvascular anastomoses are commonly performed using a series of approximately eight to ten interrupted⁶ sutures made from non-absorbable monofilament material. Figure 2.1 illustrates this technique. Advances in medical technology have enabled the manufacture of suture needles and materials specifically for this purpose, with smaller, atraumatic needles⁷ and finer, more manageable sutures. The standard suture of choice is a 9/0 or 10/0 monofilament nylon, which is mounted on a tapered non-cutting needle (25). Even in experienced hands the average time to complete an end-to-end arterial (22.3 min) and venous

⁴ Suture sizes are defined by the United States Pharmacopeia (USP). The diameter varies depending on the suture material. A USP 7/0 suture measures between 0.05 and 0.07mm.

⁵ Single fibre of synthetic material e.g. polypropylene or nylon.

⁶ Each suture is placed and tied individually i.e. not continuous.

⁷ An eyeless surgical needle with the suture permanently fastened into a hollow end.

(24.7 min) anastomosis is significant (22). With mean total ischaemic times for arteries and veins of 91.6 min and 104 min respectively (22), and an increase in clinical applications for microvascular procedures, it has become more important to discover methods of performing the anastomoses more quickly, but without affecting their overall quality.



Figure 2.1 - Demonstrating a sutured anastomosis being performed under an operating microscope

Coupled - venous

The ring-pin vascular coupling device was originally designed and reported by Nakayama in 1962 (26). This was developed for use on larger vessels in thoracic and abdominal surgery, but has been described on vessels as small as 2 mm. In 1976 Ostrup (27) conducted a study comparing anastomoses in small (2 mm) veins with sutures and the Nakayama rings. The Nakayama anastomosis was performed in one-third of the time of a sutured anastomosis and veins anastomosed by this technique had a statistically significantly lower rate of early thrombosis than the sutured veins. No difference was found in the occurrence of late thrombosis. Although this method was quicker than, and as reliable as, sutured anastomoses, it was not suitable for joining microscopic vessels as the instruments were too bulky.

In 1986 Ostrup (20) published his work on a new coupler based on Nakayama's ring-pin device. He had worked alongside Unilink⁸ to develop the microvascular coupler suitable for anastomosing vessels as small as 0.8 mm. This device has evolved into the commercially

⁸ Unilink, 3M Healthcare, 3M Center, St. Paul, MN 55144-1000, USA

available GEM Microvascular Anastomotic Coupling (MAC) System, produced by Synovis⁹, that is used today. Figure 2.2 illustrates the coupling system performing a venous anastomosis (28).

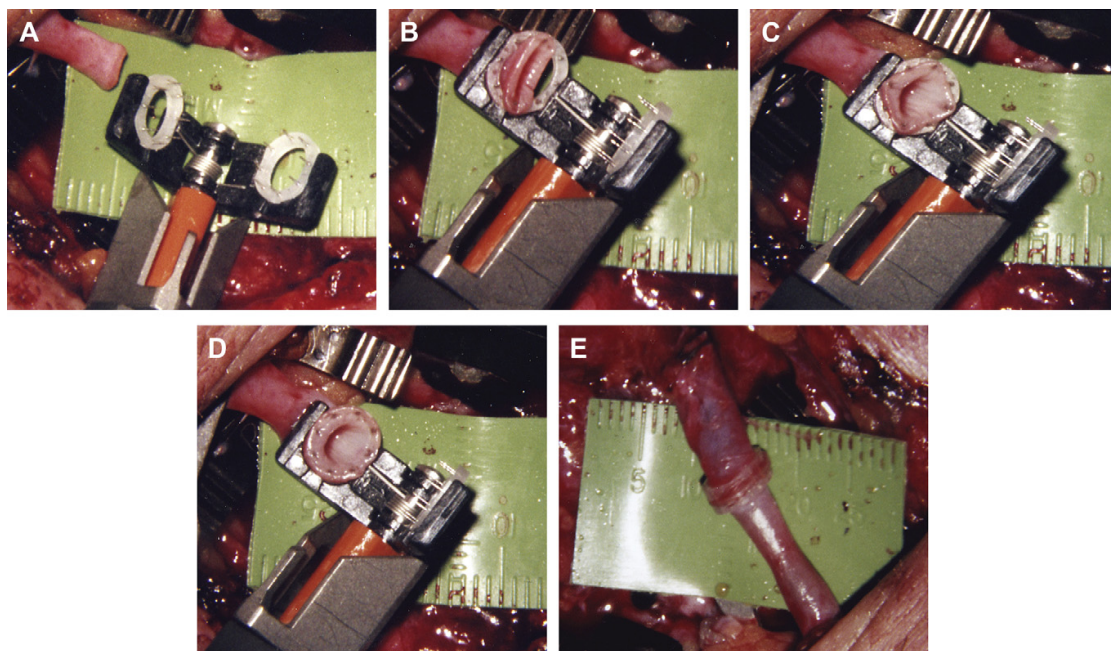


Figure 2.2 - (a) A 4.0 mm coupler in winged-jaw assembly anastomotic device, with one ring turned perpendicular to the vessel at the left that will be first attached, (b) vein initially impaled over pins at opposite ends of the major axis of the ring, (c) next, vein is everted over the pins opposite the minor axis at the ring midpoint, (d) completed fixation of vein onto all pins, (e) finished anastomosis (adapted from (28))

Since its introduction in the 1980s the MAC system (20) has been used and evaluated in many clinical studies, with the main aim of reducing ischaemic time in free flap surgery without increasing complication rates. In 1994 Ahn *et al.* (29) described their experience with the MAC system in 100 free tissue transfers, and demonstrated an overall success rate of 98.4% (121 of 123). Despite this, there were an additional 4 venous anastomoses attempted but abandoned intraoperatively due to technical difficulties. Similar results were demonstrated by Cope *et al.* (23) in 2001 that showed a 95% overall success rate, and an average anastomotic time of less than 5 minutes – significantly quicker than a hand sewn anastomosis. In 2006 a comparative study (21) of thrombosis in coupled versus sutured anastomoses was carried out which showed similar patency rates between the two techniques. Venous thrombosis rates were

⁹ Synovis Micro Companies Alliance, Inc., 439 Industrial Lane, Birmingham, AL 35211, USA

1.4% (2/139) for the MAC system and 3.3% (19/584) for hand sewn anastomoses (21), revealing reduced rates in the coupled vessels. A more recent study (30) has retrospectively analysed data on 1000 consecutive anastomoses with the MAC system and has demonstrated an overall venous thrombosis rate of 0.6%. These studies show that the MAC system is a safe and efficient alternative to sutures for microsurgical venous anastomoses, with an equivalent or better thrombosis rate.

Coupled - arterial

Although not specifically designed for use in arteries, some groups have successfully performed microvascular arterial anastomoses using the MAC system. In 2005, Ross *et al.* (31) reviewed 50 arterial anastomoses performed in head and neck reconstruction with the coupling device and demonstrated that this technique is a viable alternative to sutures. They reported a 4% (2/50) complication rate including one intraoperative thrombosis and subsequent conversion to hand-sewn anastomosis, and one anastomotic rupture due to an arterial tear (31). A further published study (32) demonstrated a large number of arterial anastomoses performed with the MAC system, also in the head and neck. A total of 127 arterial anastomoses were performed, 124 with the coupling device, and 3 which were converted to hand-sewn because of atherosclerotic plaques, inadequate flow and pseudoaneurysm formation. Of the 124 coupled arterial anastomoses, there was a 3.2% (4/124) arterial insufficiency rate and 2.4% (3/124) flap failure rate (32). Although much less common in the literature, arterial coupling for breast reconstructive surgery has been described. Spector *et al.* (33) performed 62 out of 74 (83.9%) arterial anastomoses using the coupling device with no flap losses.

Despite the coupler's apparent success in a high number of arterial anastomoses, there is a widespread consensus among surgeons that the variable patency rates and technical difficulties encountered with arterial coupling prevent it from becoming routine practice. There are several issues consistently raised in the literature which concern even the most

experienced microsurgeons, with the thicker and less distensible walls of the arteries being the most commonly implicated. These characteristics make placement of the arterial wall onto the pins challenging, often requiring a smaller diameter coupler to be used. This in turn would potentially reduce blood flow and lead to thrombosis (30). In 1994 Ahn *et al.* (29) reported a 14% (4/29) arterial thrombosis rate and 3.5% (1/29) vessel trauma rate.

2.2 Fluid dynamics

Fluid dynamics is the study of fluids in motion and, as with most physical substances, it can be investigated and analysed both theoretically and experimentally. As discussed in 1.3, fluid flow satisfies a set of basic mechanical laws and as such many fluid dynamics problems can be addressed using a theoretical approach. The main drawback of this is that the theory is based around a set of idealised situations and consequently may not be directly applicable to practical *real-life* problems.

The concept of a fluid has already been outlined in 1.3.1, and its theoretical analysis can be divided broadly into the integral, or control volume, approach and the differential approach. The control volume method determines the gross flow effects on a fluid within a finite region, where flow-in balances flow-out, whereas the differential approach describes the detailed flow patterns at each point within the fluid field (34). In addition to these theoretical analyses methods, fluid flows can also be analysed experimentally using dimensional analysis. The fundamentals of each method are outlined in this section.

2.2.1 Control volume analysis

The control volume analysis method is often based on average values at the volume's boundaries and can be applied to any flow distribution. As such, it provides a good estimate of the flow properties but is limited by the one-dimensional nature of the boundary values.

When analysing a control volume, the basic laws of the conservation of mass, energy, and momentum, are converted to apply to a specific region, which the system occupies for that instant. This is the basis of the Reynolds Transport Theorem, which can be used to analyse flow in a fixed control volume with constant or variable velocities, or even in a situation where the control volume is deformable.

Control volume or integral analysis is one of the three basic ways of approaching a fluid flow problem along with differential and dimensional, or experimental, analyses. The control volume method is concerned with the analysis of an arbitrary volume, surrounded by a geometric boundary - the control surface, through which fluid flows (16). The generalised theories of mechanics are then applied to the volume, namely the conservation of mass (equation (2.1)), momentum (equation (2.2)) and energy (equation (2.3)), in order to derive the following relationships.

$$\frac{d}{dt} \iiint_V \rho dV + \oiint_S \rho(\mathbf{v} \cdot \mathbf{n})dS = 0$$

(2.1)

$$\frac{d}{dt} \iiint_V \rho \mathbf{v} dV + \oiint_S \rho \mathbf{v}(\mathbf{v} \cdot \mathbf{n})dS = \sum_V F$$

(2.2)

$$\frac{d}{dt} \iiint_V \rho e dV + \oiint_S \rho e(\mathbf{v} \cdot \mathbf{n})dS = \dot{Q} - \dot{W}$$

(2.3)

Where ρ is the fluid density, V is the control-volume under consideration, \mathbf{v} the velocity-field vector, \mathbf{n} is the outward normal vector to the particular control surface S under consideration during the analysis; F being the body-force or surface-force depending on the integral being considered on the left-hand-side of equation (2.2). In the energy equation (2.3), e is the specific energy of the fluid, while the terms \dot{Q} and \dot{W} are the heat-transfer and work-done by the fluid, respectively (34).

It should be noted that the first term in each of the equations relates to the transient element of the relationship, whilst the second term corresponds to the surface features of the fluid. For example, in equation (2.1) the term $\frac{d}{dt} \iiint_v \rho dV$ represents the mass in the control volume at any given point in time. The second term, $\iint_S \rho(\mathbf{v} \cdot \mathbf{n})dS$, indicates that the mass flow rate at each of the control surfaces remains conserved.

2.2.2 Differential analysis

The differential analysis method examines the details of a flow pattern by analysing an infinitesimal region of fluid flow. The basic conservation laws are applied to an infinitesimal control volume to produce the differential equations of fluid motion (35). Applying these important principles to an infinitesimal control volume detailed in equations (2.1) to (2.3), renders the appropriate Partial Differential Equations (PDEs) of fluid motion, which are subsequently solved by the CFD code. Of particular importance to this work are those of mass and momentum:

$$\frac{\partial \rho}{\partial t} + \frac{\partial}{\partial x}(\rho u) + \frac{\partial}{\partial y}(\rho v) + \frac{\partial}{\partial z}(\rho w) = 0$$

$$\frac{\partial \rho}{\partial t} + \nabla(\rho \mathbf{v}) = 0$$

where nabla (∇) is the mathematical gradient detailing the change in the mass across each infinitesimal control surface within the flow-field. Since the benchmark and vascular simulations all use incompressible fluids (typically water or blood), then these equations reduce to:

$$\nabla \mathbf{v} = 0$$

(2.4)

In all the simulation work that follows, due to the nature of the working fluid operating at velocities with negligible Mach numbers, it is this equation that is solved together with momentum (Navier-Stokes), thus establishing the primary solution velocity vector.

In addition to these equations, the viscous stresses of the fluid must be accounted for. The Navier-Stokes equations incorporate the viscous nature of the fluids in question and can be derived (35) via an appropriate momentum balance of an infinitesimal control volume, as defined in section 2.2.1, coupled with the definition of the Einsteinium stress tensor (36). This is used to obtain a PDE that makes volumetric mass and acceleration equal to the volumetric gravity (\mathbf{g}), force (pressure) and viscous forces. Finally, for Newtonian fluids (18) the definition of the of viscosity renders:

$$\rho \frac{d\mathbf{v}}{dt} = \rho \mathbf{g} - \nabla p + \mu \nabla^2 \mathbf{v}$$

(2.5)

which are the Navier-Stokes equations in their compact form. It should be noted here, purely for completeness, that equation (2.5) actually denotes *three* PDEs (35) one for each of the principal directions of motion in this case the principal orthogonal set. It is these three equations that are solved together, along with that of continuity (2.4), in the CFD software.

The advantages of this method over the control volume analysis are that it permits point-by-point knowledge of the flow field, and that it is valid for any flow in any motion. The disadvantage of this method is that the differential equations derived are inherently complex and contain nonlinear terms, which further complicates the mathematical analysis.

Fortunately, the advent of CFD has made solving these lengthy equations much simpler and quicker. That is, modern commercial CFD code such as that employed in this work takes away much of the mathematical complexity via the use of sophisticated numerical routines which

solve the continuity and Navier-Stokes equations. The validity and convergence of solutions obtained can be verified in some part via appropriate plots of the convergence norms resident in the software. These should always be used in conjunction with appropriate simplistic analogous analytical solutions and, where possible, empirical data (37,38); which is the case in the work that follows. In the case of the analytical model formulations it is usually necessary to re-cast the governing equations of fluid flow namely, equations (2.4) and (2.5), in to cylindrical coordinates which are polar coordinates extended into three-dimensions represented by r , θ and z (39) as shown in Figure 2.3; here only steady-state solutions are considered, where the first term in equation (2.5) can be removed.

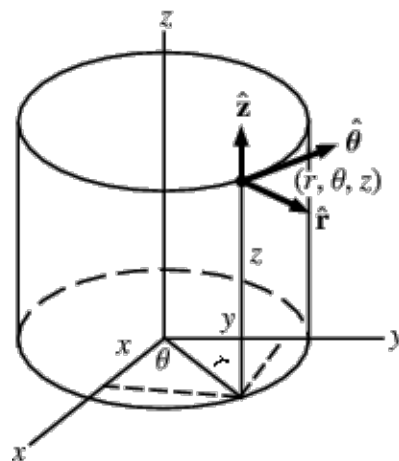


Figure 2.3 – Illustrating the cylindrical coordinates (from (39))

It is worth noting that whilst the Navier-Stokes equations can be applied to evaluate Newtonian fluids, where the viscous stresses are proportional to the element strain rates and the coefficient of viscosity (35), Euler's equation (35) can be applied to evaluate inviscid flows. Euler's equation can be derived from equation (2.5) by removing the viscosity term, where, in the absence of gravity (which is the case here, as the pressure to maintain blood flow within the vessel would render gravity negligible):

$$\rho \frac{dv}{dt} = -\nabla p$$

(2.6)

This is useful in the inspection of flows that may be considered distant from the boundary layer, for instance, the central streamlines in the blood vessel models considered within this thesis.

2.2.3 Dimensional analysis

Dimensional analysis is a method for reducing experimental data to a minimum data set, which is dimensionless. It reduces the number and complexity of experimental variables using a compacting method. Dimensional analysis also has other perceived advantages in that it saves time, aids in the planning of an experiment, and provides a set of scaling laws by which a scale model can be converted to a prototype. Although this method is likely to provide some of the most *real-life* solutions, it would be impossible to apply to the current research problem due to the microscopic nature of the fluid domain. Rickard *et al.* (40) did use transit-time ultrasound to measure the overall flow-rates of blood through analogous vessels in a rat model, but this method is too insensitive to examine local flow phenomena around defects within the vessel lumen seen in sutured and coupled anastomoses.

2.3 CFD

CFD codes model fluid flow through a particular domain by breaking it down into a fine mesh consisting of volumes and nodes. The code's solver then solves the PDEs for each of the thousands or even millions of volumes within the mesh to produce a numerical solution. CFD therefore allows engineers to analyse fluid flow problems in a wide variety of environments including the industrial, motorsport, and medical fields. The greatest advantage of CFD is the ability to simulate flow and create numerical results in otherwise expensive and time-

consuming experiments, or in those circumstances that would be impossible to recreate experimentally, such as the work described in this thesis. The main disadvantage of CFD is that the potential for errors and obtaining inaccurate results are great. CFD should therefore be used in conjunction with experienced computational engineers with a firm understanding of fluid mechanics and should be applied to appropriate problems in order to obtain realistic solutions.

2.3.1 Fundamentals

CFD methods are concerned with the solution of the equations of motion for fluids. The first step in CFD is to input or create a geometry that is representative of the fluid domain to be analysed. This can be generated either within the software itself, or imported as a scale model from a Computer Aided Design (CAD) package, or even from a high-resolution scan or photograph.

In a pre-processing stage the geometry is then divided into a mesh to enable numerical analysis of the domain. The mesh is created in such a way that the domain is completely covered by the mesh, there is no space left between the mesh cells, and that the mesh cells do not overlap each other. The user can define the mesh density and, generally, finer meshes yield more accurate data. The resulting mesh is described computationally as a series of coordinates from which the millions of control volumes are defined (38). The governing equations are then solved for each of the control volumes.

The equations of motion of an inviscid fluid (Euler equations) and of viscous fluid (Navier-Stokes equations) are solved for each model to provide approximate computer-based data. The Navier-Stokes equations provide accurate solutions for laminar viscous flows, but are less useful in a turbulent model. The Reynolds-averaged Navier-Stokes equations offer a simple and more accurate method of turbulence modeling, however the Reynolds stress model provides an even more detailed data-set when considering turbulence (38).

The governing equations mentioned above are the same no-matter what type of fluid problem they are applied to, however it is clear that not all fluid problems are the same. The way in which CFD distinguishes between these is via the boundary conditions. For viscous flows the surface boundary condition assumes no relative velocity between the surface and the fluid – known as *non-slip* conditions. For inviscid flows however, there is no friction at the fluid-surface boundary and the fluid slips freely at a tangent to the surface (41). The remaining boundary conditions depend on the fluid problem being addressed, but usually comprise of an inlet and outlet at specific points.

Once the model has solved, data are created by the CFD code can then be analysed and examined in the post-processor within the analysis software.

2.3.2 CFD and blood flow modelling

Flow modelling and computing have been extensively used to develop a detailed understanding of local blood flow patterns within vessels since the link between altered blood vessel haemodynamics and the formation of atherosclerosis¹⁰ was made. The first connections between haemodynamic forces and atherosclerosis were established in the 1980s by Friedman *et al.* (42) who used laser Doppler velocimetry to examine blood flow in human arteries and correlate this with areas of atherosclerosis post-mortem. Casts were made of the aortic bifurcation of a male with atherosclerosis and a laser Doppler anemometer was used to measure fluid velocities in the cast at selected sites. Intimal thickness was measured at corresponding sites and a negative correlation was found between intimal thickness and wall shear rate (42). In the early 1990s, CFD emerged as a technique for investigating local flow patterns in extreme detail, making more sophisticated studies possible (43,44). Additionally, Perktold (45–48) and colleagues were responsible for the majority of the novel work in this field, and were the first group to demonstrate the carotid bifurcation using CFD. Their carotid

¹⁰ Atherosclerosis is a disease of the arteries in which fatty plaques and scar tissue form in vessel walls causing degeneration. This can limit blood flow and predispose to thrombosis.

bifurcation was actually based on a geometry created by Ku *et al.* (49) who used human angiograms to construct a Plexiglas model which was scaled upwards by 125 times to permit analysis of flow using a high resolution laser Doppler. Perktold *et al.* (48) used the original dimensions taken from the angiograms and applied incompressible Newtonian fluid characteristics along with the calculated flow rates obtained from the work of Ku *et al.* (49). The computational numerical analysis performed by Perktold *et al.* (48) confirmed the flow fields and mechanical stresses found by Ku *et al.* (49) in their up-scaled experimental Plexiglas model.

The increasing availability of CFD as a research tool, combined with ever-improving computer capabilities, led to a multitude of studies into the local haemodynamic flow within vessels. Factors such as low wall shear stress (49), flow disturbance (50), high oscillatory shear stresses (51), and vessel wall tension (52) were all implicated as factors affecting atheroma formation through the use of CFD. These correlations are supported by studies carried out in animal models by DePaola *et al.* (53) who demonstrated that large shear stress gradients could induce morphological and functional changes in the endothelium in regions of disturbed flow. Bryant *et al.* (54) have also shown vascular remodeling in response to altered blood flow *in vitro* and have implicated fibroblast growth factor-2 (FGF-2) as its mediator.

As well as developments within CFD, significant improvements were also being made within medical imaging. This led to *in vivo* measurements of haemodynamics using techniques such as Doppler ultrasound (55), Magnetic Resonance Imaging (MRI) (56), and angiography (57). It then became possible to combine CFD with image-based techniques to investigate realistic vascular geometries (58–60). Detailed reviews of the developments of image-based modelling of blood flow over the last two decades have been carried out by Steinman (61) and Taylor (62).

In the early days of CFD, simulations initially required several days of computer processing and could only produce two-dimensional models of idealised geometries. Now however, it is

possible to convert detailed high quality medical images into complex three-dimensional meshes for simulation of blood flow in individualised patients (63). This process involves contrast-enhanced Magnetic Resonance Imaging (ceMRI) of the vessels and the application of a computational filter to calculate flow rates. The ceMRI images are converted into a mesh and then a patient specific flow simulation is created using a CFD solver (63). Although these simulations are clinically relevant and can be used to aid therapeutic decision making for certain pathologies, for example aortic dissection, some limitations still exist. These are primarily related to assumptions made in order to reduce processing time of large volumes of information, including arterial wall non-slip conditions, rigid walls, and blood as a Newtonian fluid (63).

Application of CFD to blood flow within vessels, whether pristine or pathological, is complex, but the addition of a surgical anastomosis creates further issues for consideration including compliance mismatch, new geometries and subsequently new local haemodynamics (64). Several studies have been carried out to model flow in a range of anastomoses both in large and small vessels.

Coronary Artery Bypass Graft (CABG)

The first computational models of CABG end-to-side anastomoses were carried out in the early 1990s and were based on two-dimensional steady-state simulations (65,66). The following decade saw the introduction of pulsatile flow (67) and three-dimensional modelling incorporated from MRI (68).

Peripheral Artery Bypass

As for modelling in CABG, early computational models of peripheral bypass anastomoses were created in the 1990s (69) and were simplified greatly in comparison to current techniques. Studies into end-to-side bypass grafts increased markedly with increasingly more detailed models being created. The works of Lei *et al.* (70–72) have explored the incorporation of vein patches to prosthetic vascular grafts, and proposed CFD based design alterations to minimise

Wall Shear Stress (WSS) gradients. A comprehensive study was carried out by Perktold *et al.* (73) examining the different compliance of synthetic grafts, arterial walls and the presence of suture material. This extensive study compared these factors in conventional anastomoses as well as in those with a vein patch, and then performed an *in vivo* comparison in a sheep model. Although this study has used CFD to model suture lines, it has only investigated the principal stress contours at the suture site and has not examined local flow patterns around the suture itself.

Microvascular Anastomoses

There has been little work in this area, with only a few studies carried out to investigate the computational modelling of microvascular anastomoses. Al-Sukhun *et al.* (74) developed a finite element model (FEM) to study the effect of stress and strain in microvascular anastomoses. This group created FEMs of end-to-end and end-to-side anastomoses and also included a simulation of size discrepancy between the host and recipient vessels. The principle finding of this study was that the effect of discrepancy in the size of the vessel in end-to-end anastomoses was remarkable, with a reduction in blood flow of 48 ml min^{-1} , when compared to end-to-side anastomoses, with a reduction of only 11 ml min^{-1} (74).

A second study into the computational modelling of microvascular anastomoses was that of Rickard *et al.* (40) who investigated several techniques for anastomosis in arteries with size discrepancy. Four idealised end-to-end anastomotic techniques were modelled where the recipient artery was smaller. Flow data were acquired via transit time ultrasound of the exposed femoral artery of a Wistar rat – a vessel similar in size and structure to that of a human internal mammary artery (IMA) perforator used for microvascular anastomoses in breast reconstruction. CFD modelling was performed to evaluate flow patterns and WSS in the idealised anastomoses, with the ‘wedge’ technique proving the best construct demonstrating the least flow separation.

The above studies have evaluated in detail the WSS and flow through idealised microvascular anastomoses, but neither have investigated the local haemodynamics around sutures, or have explored the flow patterns through coupling devices.

2.3.3 CFD software codes

There is a range of commercial CFD software codes available to perform computational fluid flow analyses. Amongst the literature reviewed in this thesis, there were five main commercial codes used in a similar context to this study i.e. to model blood flow in vessels. These are shown briefly in the list below and are then subsequently outlined in more detail:

- Rickard (40) and Karmonik (63) used ANSYS Fluent
- @neurIST study (75) used ANSYS CFX
- Chaniotis (76) used STAR-CD
- Antiga (60) used the Vascular Modelling Tool Kit (VMTK)
- Perktold (73) used ABAQUS

ANSYS Fluent is a commercial CFD code provided by ANSYS Inc. that contains the broad physical modelling capabilities needed to model flow, turbulence, heat transfer, and reactions for industrial applications. It has advanced solver technology, which provides fast, accurate CFD results for flexible moving and deforming meshes. ANSYS Fluent has an interactive solver setup, solution and post-processing capability, which makes the modelling process straightforward and intuitive (77). It has been used reliably to model blood flow in vessels (40,63).

ANSYS CFX is a high-performance, general-purpose fluid dynamics code that has been applied to solve wide-ranging fluid flow problems for over 20 years. Like ANSYS Fluent, it too has advanced solver technology, which produces reliable and accurate solutions quickly and robustly (78). It can capture virtually any type of phenomena related to fluid flow and has been used successfully by an international study on intracerebral blood flow when analysing flow within small cerebral aneurysms (75).

STAR-CD is a high-performance CFD environment that can perform reliable analysis of complex, multiscale transport phenomena in realistic industrial systems, usually internal combustion engines. STAR-CD is well suited to the solution of large-model simulations and features a well-integrated platform for creating models from concept, or body-fitted meshes from existing CAD geometry models (79). It has robust solver technology for multi-physics simulations involving turbulence, heat transfer, and multiphase flows. Chaniotis *et al.* (76) utilised STAR-CD to analyse their models of coronary vessels with reliable results.

The VMTK is one of the only specific CFD packages designed for the analysis of vessels from medical images such as CT or MR scans. VMTK is able to perform geometric analysis and surface data processing of 3D models of blood vessels, and has an integrated mesh generator and editor. Its pre-processor allows creation of surface boundaries and boundary layers (80). It was created by David Steinman and Luca Antiga (60), who have both used VMTK to analyse flow in blood vessels.

ABAQUS provides advanced, scalable and parallel, CFD for a broad range of simulations. Both external and internal flows of complex geometries that are in steady state or transient conditions can be simulated over a wide Reynolds number range. Thermal convective simulations involving heat transfer such as natural convection can also be simulated (81). Perktold (73) successfully used ABAQUS to simulate fluid dynamics in peripheral bypass anastomoses.

This study uses ANSYS CFX to analyse blood flow through microvascular anastomoses. ANSYS CFX was chosen for several reasons. Firstly, it is a well-established and well-respected CFD code in the industrial setting, including cutting-edge technologies such as Formula 1 and nuclear engineering; secondly, it has been used in a previous internationally recognised study on simulated blood flow in small vessels in humans (75); thirdly, the University of Central Lancashire has access to ANSYS CFX and has a team of staff who are proficient at its use; and finally ANSYS Inc. has an excellent training and support facility which is accessible via the

University. From a technical point of view, ANSYS CFX is a reliable code that has a high quality mesher and is able to produce accurate solutions rapidly when compared to other commercially available codes.

2.4 Boundary conditions and material properties

Determining the correct boundary conditions and material properties for a simulation is key to obtaining accurate, reliable and comparable results. To this end, several studies were evaluated to obtain the most appropriate and applicable boundary conditions for this research.

Boundaries in CFD are essentially grouped into two, namely walls that encompass the fluid domain, and openings through which flow enters or exits the domain. Openings are further subdivided into inlets and outlets.

There is an agreement amongst several studies (40,63,73,77), including an international study on intracerebral blood flow (75), that walls may be simulated as rigid, non-compliant structures with non-slip conditions. This is likely to be due to technical difficulties modelling fluid-solid interactions to produce physiologically accurate boundaries. As such, the majority of the studies have knowingly compromised when devising their models in order to gain an appreciation of the flow patterns, rather than the most physiologically accurate results.

Inlet properties varied depending on the models used, however, a consistent feature amongst the studies (40,76) was the use of either a velocity or mass flow rate at this opening. For outlets, a pressure boundary condition is applied (40,76). Actual figures for inlet and outlet properties used in this study are detailed in sections 3.3.1 and 3.3.2, respectively.

The material properties of blood itself are largely well established in the literature. Blood is considered an incompressible fluid and as such will have a constant density. There is minor

variation in the density figures quoted in the literature ($1052\text{-}1064\text{ kg m}^{-3}$)(83), however, several studies have used a figure of 1060 kg m^{-3} (40,75,76), which has also been adopted for this research.

One of the main considerations that has been debated in the literature is whether to model blood as a Newtonian or non-Newtonian fluid. Many studies have investigated this within vessels of varying sizes under a range of conditions. Overall, it appears that, under standard conditions, in blood vessels of the dimensions that will be studied in this project, the non-Newtonian nature of blood is not significant (76,84). One paper (85) compared seven non-Newtonian models and one Newtonian model in evaluating flow through cardiac vessels, and found that Newtonian flow was considered a good approximation at mid and high-strain rates. However, not all studies entirely agree. Chen and Lu (86) investigated non-Newtonian flow in a pulsatile model and demonstrated a significant difference between Newtonian and non-Newtonian flow during the pulse cycle. Despite this, during a rheology study carried out by Bernsdorf *et al.* from the @neurIST group (75), it was demonstrated that the non-Newtonian Carreau Yasuda model yields different solutions to those obtained with a Newtonian model, but that the differences were most pronounced at unphysiologically low Reynolds numbers. At a Reynolds number of 100, still at the low end of the physiological range, Bernsdorf reports relatively small differences for the peak shear stress on the walls for Newtonian and non-Newtonian models (75). In keeping with the protocols for the @neurIST (75) study and those of Rickard *et al.* (40), blood has been modelled as a Newtonian fluid in the research described in this thesis.

Viscosity figures are also largely consistent within the literature with a range from 0.0035 Pa s (75,76) to 0.0050 Pa s (40). In the modelling protocol by Berti *et al.* (75) consideration was

given to the average haematocrit¹¹ which yielded 0.0035 Pa s as the figure for the viscosity for their simulations; this figure will be used in the present study.

2.5 Flow effects and blood coagulation

Although low blood flow and stasis within vessels are risk factors for thrombus formation, it is known that Shear Strain Rate (SSR) is a more reliable factor to evaluate than flow rate or flow velocity when evaluating coagulation in the presence of flow (87). This is because SSR governs the transport phenomena near the surface of vessels and describes the change of flow velocity with increasing distance from the surface (88).

As previously mentioned in 2.3.2, WSS has been implicated as a factor leading to atheroma formation within blood vessels (49,53,89,90). More importantly for this research, high WSS and SSR have also been strongly linked to platelet activation (91–94). This is particularly important when considering blood coagulation and thrombosis, as activated platelets adhere to each other to form aggregates, and subsequently thrombus. In addition, shear-induced platelet thrombus formation appears to promote the generation of fibrin¹² through the activity of soluble coagulation factors (95). Excessive generation of fibrin also leads to thrombosis. Interestingly, shear-activated platelets do not appear to adhere to an intact vessel wall endothelium (96), but they do bind tightly to injured endothelium and exposed subendothelium (87). It is possible this may be more important in sutured anastomoses than in coupled anastomoses as there is a greater chance of exposed subendothelium in the sutured technique, both from the suture sites themselves and from the cut vessel ends, however this has not been validated. The exposed subendothelium in the coupled anastomosis is reflected backward and outward, to allow intima-intima contact (97), and as such is not in contact with the intravascular blood flow.

¹¹ The percentage volume of red blood cells

¹² Fibrin (also called Factor 1a) is a fibrous, non-globular protein involved in the clotting of blood.

Shen *et al.* (93) and Roth (94) demonstrated that SSR of greater than $\approx 1 \times 10^3 \text{ s}^{-1}$ cause direct activation of platelets. A recent computational study (98) found a positive correlation between thrombus accumulation rates and SSR up to $6 \times 10^3 \text{ s}^{-1}$. This study also showed that thrombus growth rates were two to four times greater at higher SSR than for physiological shear rates of less than 400 s^{-1} (98).

2.6 Introduction of methods

Although there is a wide range of literature available on the subject of CFD and blood flow modelling, only a small number of studies are directly applicable to this research. In particular the work of Rickard *et al.* (40) in his study of microarterial anastomoses in vessels with size discrepancy, demonstrate logical experimental method with clinically relevant simulation parameters. In addition, the work of Berti *et al.* in the @neurIST study (75) employs very similar physical modelling parameters and uses clinically applicable image-based geometries for the analysis.

The simulation strategy for this research has been based on the methods of these studies as they are investigating similar blood flow patterns in comparable sized vessels. Both research groups have been successful at demonstrating their findings in the international research community and this project intends to do the same.

The modelling strategy followed a logical sequence, starting with simple models of circular ducts with a known fluid (i.e. water) and moving to progressively more detailed and clinically relevant models of microvessels with blood as the working fluid.

In order to ensure that the blood vessel simulations generated accurate results, it was important to ascertain that the results produced by the ANSYS CFX software were correct. The

first step was to perform an appropriate benchmarking study using a basic duct of 1 mm in diameter and to simulate flow through it using water.

There was a good agreement between the expected analytical, empirical and CFD numerical results. Blood then replaced water as the fluid for analysis, using data from the literature and assuming it to be an incompressible Newtonian fluid. In addition, a laminar flow regimen was employed due to the low Reynolds number in these models.

Geometries were then created to replicate idealised sutured and coupled anastomoses.

Adding a circumferential sequence of ten tori with the same dimensions as a microvascular suture created the sutured anastomosis. The coupled anastomosis process was performed in computational space using the Computer Aided Interactive Three-dimensional Application (CATIA) commercial Computer Aided Design (CAD) and analysis code.

Simulations were carried out using steady-state analysis in this thesis, however it was intended that transient models would be created to mimic the pulsatile nature of blood flow *in vivo* in subsequent work, section (6.2). Flow rates for the arterial models were obtained from the literature (see 3.3 for details), and pristine, sutured and coupled anastomosis simulations were then performed.

3 Methods

This chapter describes the simulation strategy for this research along with the methods of geometry creation and meshing techniques. The application and justification of appropriate boundary conditions are also presented.

3.1 Vessel fluid geometry creation

All geometries were created in the ANSYS DesignModeler application within the ANSYS Workbench (v13) software, and were designed with longitudinal symmetry exploited. This *half model* strategy was employed for two reasons. Firstly, it allowed direct visualisation of the internal flows after analysis, and secondly, it permitted the application of a symmetry condition, which reduced the computational demand and thus reduced simulation time. In keeping with previous work (40), all vessels were modelled with a diameter of 1 mm to maintain continuity and clinical relevance. All vessel geometries were also kept at a constant length of 5 mm, with the anastomosis being at the centre-point, which was chosen to allow good visualisation of the flow into and out of the anastomosis region. It was deemed unnecessary to model vessels longer than 5 mm as a paraboloid velocity profile was added to the inlet to ensure fully developed flow prior to the anastomosis (see section 3.3.1)). In an attempt to ensure the most accurate analysis of the anastomosis, a finer mesh was applied to the anastomotic site.

3.1.1 Pristine model

The pristine model was constructed by initially creating a semicircle with a diameter of 1 mm in the *xy*-plane. This was then extruded to form a hemi-cylinder with a diameter of 1 mm, and length of 5 mm, as shown in Figure 3.8(a).

3.1.2 Sutured anastomosis

The sutured anastomosis was created using DesignModeler's primitive three-dimensional objects. An ANSYS DesignModeler primitive torus was used to mimic the suture and was given the same dimensions as microvascular suture material (0.03 mm). This was then replicated nine times, to model ten separate sutures, circumferentially at the midpoint of the aforementioned pristine geometry (see Figure 3.8(a)). This ring of sutures was then subtracted from the previously created pristine geometry by employing a subtraction body operation resident in DesignModeler. This operation essentially removed the tori thus leaving a hemicylinder with suture-like deformities in an equidistant, concentric pattern. This process is depicted below in Figure 3.1.

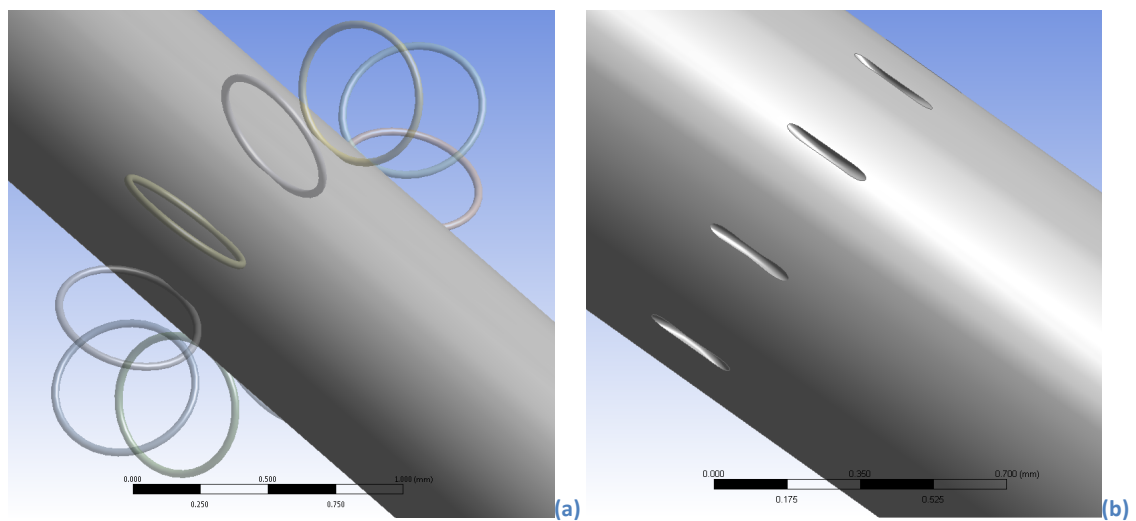


Figure 3.1 - Suture three-dimensional modelling process (a) tori ring (b) subtraction body operation

3.1.3 Coupled anastomosis

The coupled anastomosis was created initially using measurements taken from the coupler components under a microscope, with the sizes of the required fluid volume extracted from a CATIA model as shown in Figure 3.2.

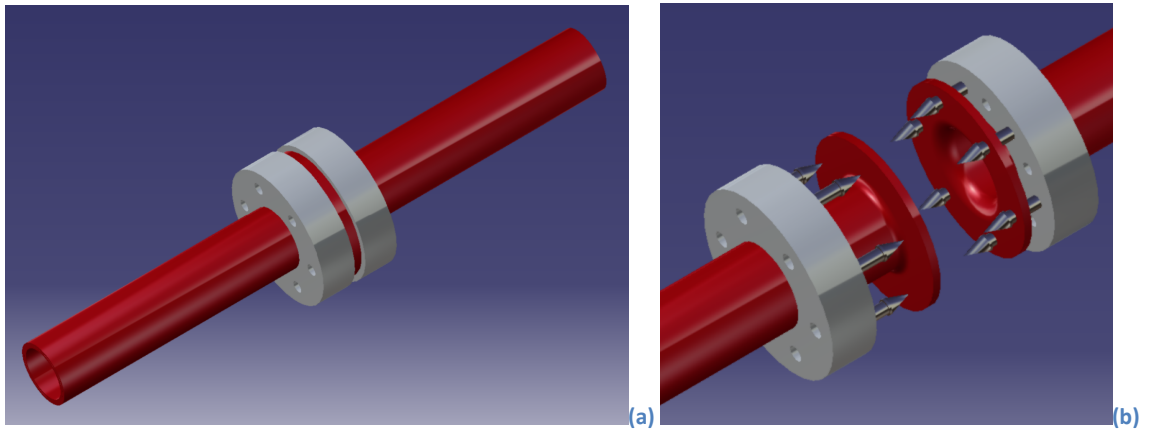


Figure 3.2 - CATIA coupled anastomosis (a) assembly (b) exploded assembly

This CATIA model (Figure 3.2) was constructed using the *Mechanical Assembly Design* workbench resident in the software using three previously formed CATIA *parts*, namely: coupler-flange, pin and vessel section as shown in Figure 3.3.

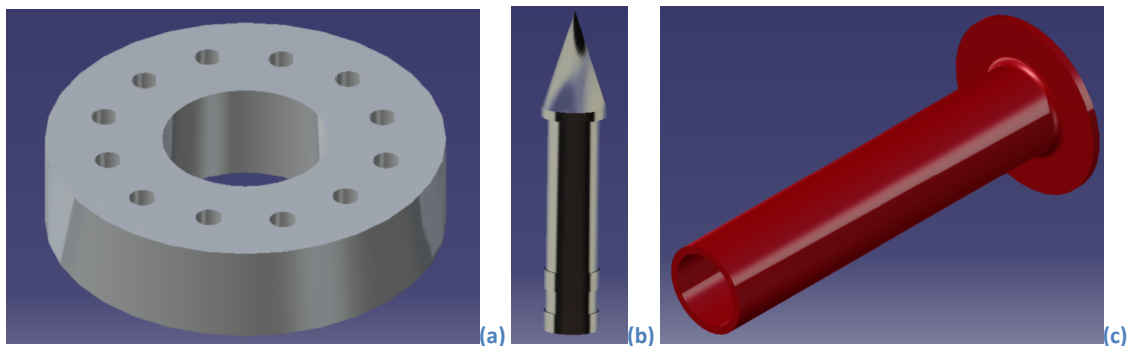


Figure 3.3 - CATIA anastomosis assembly parts (a) coupler flange, (b) pin and (c) vessel section

The coupler flange was modelled using the sophisticated sketch tracing facilities supported by CATIA. The exact geometrical form of the whole coupling device was extrapolated from micrographs shown in Figure 3.4. Here the CATIA software extrapolated the smaller dimensions (e.g. pin holes) from the principal dimension of the known internal diameter of 1mm. Then, using the *Part Design* workbench, the inside and outside diameters were extruded using the CATIA-Pad command. A single hole was then positioned on a pitch circle diameter equivalent to the average of the inside and outside diameters; the diameter of the hole being extrapolated by CATIA as described previously. Finally, this *part* design was completed via the production of an array.

Thereafter, the CATIA *Image and Shape* workbench was employed for extrapolation of the pin length from the micrograph shown in Figure 3.4(b), in addition to other principal sizes. The pin being completed in three-dimensional space via a simple revolve using the CATIA-Shaft command in the *Part Design* workbench.

The vascular section was constructed from a single revolution using the CATIA-Shaft command in order to produce a vessel with an outside nominal diameter of 1 mm, and reflected vessel wall of suitable size to effectively use the coupler flange. Subsequently, a wall-thickness (0.1 mm) (99) was added to this initial surface model to produce the finalised three-dimensional CATIA part.

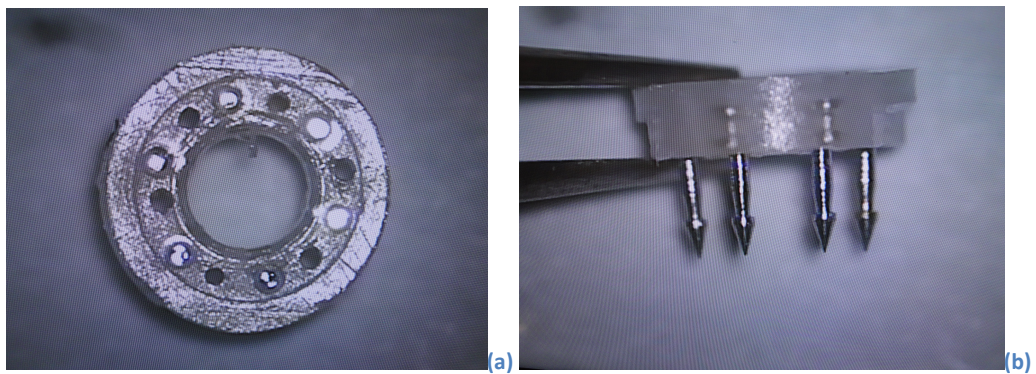


Figure 3.4 - Micrographs of coupling device (a) plan and (b) side elevation used to construct CATIA model

A sub-assembly was constructed in the CATIA *Mechanical Assembly Design* workbench that consisted of the coupler flange and six pins (Figure 3.5). This was achieved by using a *coincident* constraint between the axes of each hole and pin. In addition a *surface contact* constraint was applied at the base of the pin and hole; in each of the positions depicted in Figure 3.5.

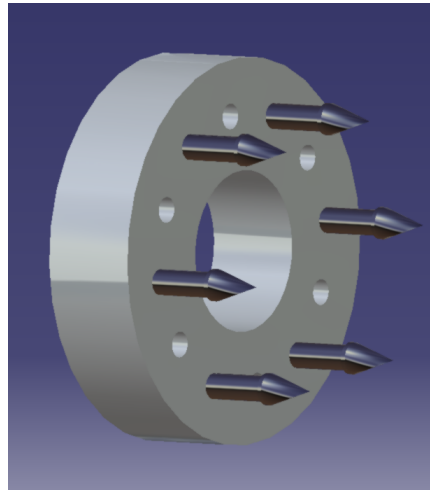


Figure 3.5 - CATIA coupler sub-assembly

The surgical microvascular coupling procedure was then simulated using the CATIA Mechanical Design Assembly workbench. In essence the actual surgical operation was replicated using the CATIA functionality. Here, an analogous method was employed as that used to produce the coupler sub-assembly. The vessel and coupler sub-assembly were made coincident along the longitudinal axis, and a surface constraint applied between them, as indicated in Figure 3.2(b). This procedure was repeated for a second vessel and coupler, which were aligned using appropriate coincident constraints on the remaining pins and holes, and subsequently interlocked, as would be the case in the actual surgical procedure.

With the anastomosis assembly model completed, the fluid control volume was determined by sectioning the model through the axis of the vessel horizontally as shown in Figure 3.6(a) and (b). The fluid volume was created by revolving half this section about the longitudinal axis as can be seen in Figure 3.6(c).

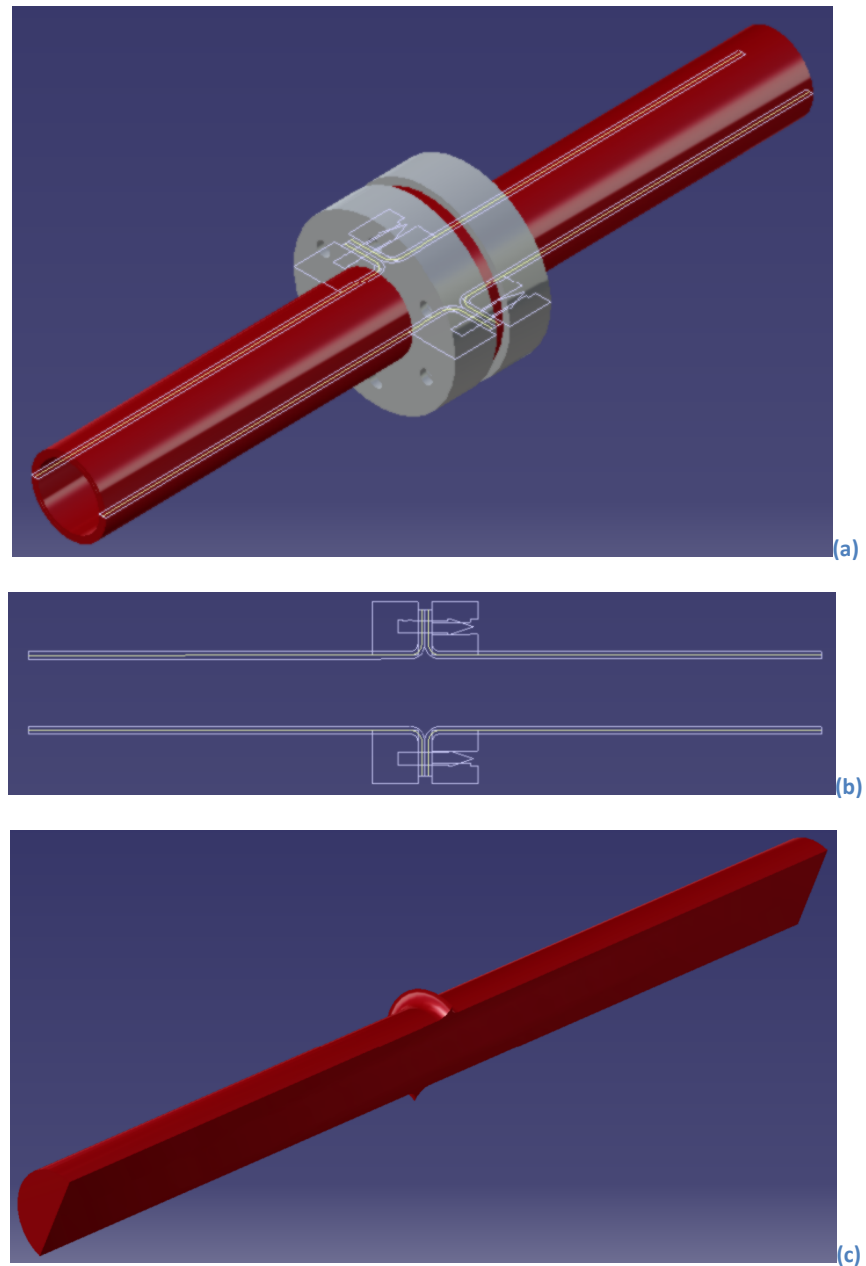


Figure 3.6 - Control volume creation (a) section creation, (b) resulting section and (c) symmetric fluid volume

Hence, the coupled anastomosis fluid model consisted of an annular outward-facing deformity to mimic the reflection of the vessel walls when the coupling device was *in-situ*. The CAD image of the anastomosis was then transferred manually into ANSYS DesignModeler, and the wall defect re-created. The luminal diameters of the sutured and coupled models were scaled and standardised to 1 mm during the ANSYS simulations to ensure direct comparability.

3.2 Meshing techniques

All geometries were meshed using ANSYS Meshing (v13). Following advice directly from ANSYS Inc. regarding the meshing of small ducts, and also in keeping with a large international study using CFD to model cerebral aneurysms (75), tetrahedra meshes were created for all geometries. The crucial aspect of this research was to monitor as closely as possible the flow profile close to the walls, sutures and coupler. To this end, the patch conforming meshing technique was used. This created a detailed surface mesh first, and then formed the volume mesh. In a further attempt to ensure the most accurate readings at the model's periphery, a fine high-density mesh was then applied. All meshes were set with high smoothing to create the smoothest transitions between mesh cells.

As described in Section 3.1, the central (anastomosis) section of each geometry underwent a further mesh refinement at the model edges in order to capture the boundary layer flow field. Mesh reports for the geometries, along with target figures as suggested by ANSYS (100), used in this study can be found below in Table 3.1. This clearly showed that the number of nodes and tetrahedra increased as the complexity of the geometry increased.

	Nodes ($\times 10^3$)	Tetrahedra ($\times 10^6$)	Min. Face Angle (Target $\geq 10^\circ$)	Max. Face Angle (Target $\leq 170^\circ$)	Edge Length Ratio (Target ≤ 100)
Pristine	75	0.04	12°	143°	5
Sutured	393	2.08	10°	147°	5
Coupled	460	2.41	8°	146°	7

Table 3.1 - Mesh reports for vessel geometries

Given the microscopic nature of the simulations being performed, it was paramount to ensure maximum accuracy by minimising the sources of error. One potential key source of error was

poor geometrical mesh quality. Mesh quality could be measured in several ways i.e. mesh orthogonality and aspect ratio (or stretching).

Mesh orthogonality relates to how close the angles between adjacent element faces are to an optimal angle and can be measured using a variety of techniques, one of which is the maximum and minimum face angle. As shown in Table 3.1, all models have maximum and minimum face angles in the ideal range except for the coupler, where the minimum face angle is 8° , and ideally should be 10° or above. Although this was outside the ideal range, it was by a very small amount, and the face angle parameter is not always optimal in three-dimensional flows. As such, the figure of 8° was deemed acceptable and unlikely to cause significant error.

The mesh aspect ratio relates to the degree that mesh elements are stretched, and can be measured using the edge-length ratio. Again, referring to Table 3.1, all meshes from the vessel geometries had edge-length ratios well within the acceptable range.

These methods of mesh quality control indicated that reliable, good quality geometries have been created and as such, reliable results should be obtained. Detailed figures of the sutured and coupled meshes are shown in Figure 3.7(a) & (b) and (c) & (d) respectively with images of all three vessels shown in Figure 3.8. It should be noted that whilst the mesh densities at the anastomotic regions of each vessel appear different, they have undergone identical refinements as dictated by the ANSYS CFX software.

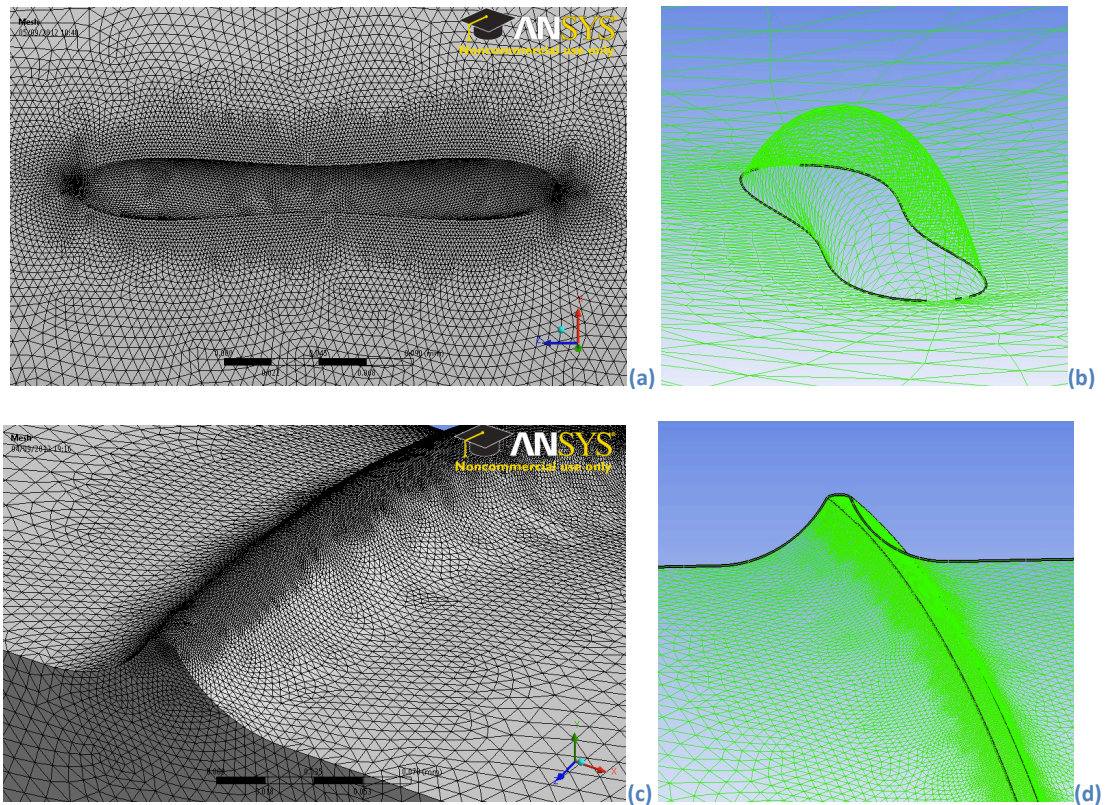


Figure 3.7 - Meshes of the anastomotic region in the sutured (a) & (b) and coupled (c) & (d) models

3.3 Boundary conditions

Each model required a detailed set of accurate boundary conditions to be applied so that the correct conclusions could be drawn from the results obtained. Two principal types of boundary conditions were applied to the models, namely at the walls surrounding the flow domain, and at the openings through which flow entered or exited this domain. Each boundary surface of the geometry was addressed separately, as follows:

3.3.1 Inlet

The inlet boundary conditions remained constant for all simulations including the benchmarking studies and vessel model analyses. These will now be explained individually. From a mathematical viewpoint, they can be thought of as the knowns required in the Reynolds transport equations (2.1) and (2.2) in order to solve the resulting system, e.g. the Navier-Stokes which follow. The inlet location is shown in Figure 3.8(a).

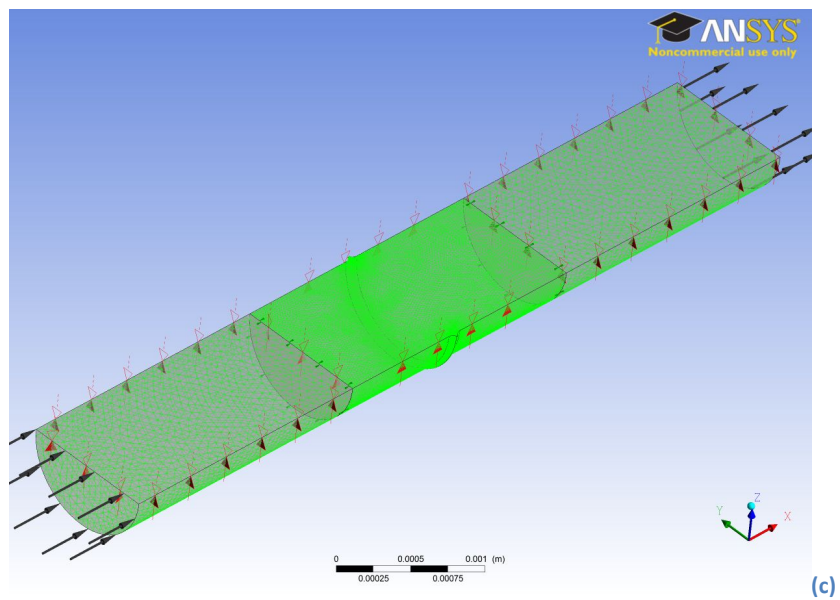
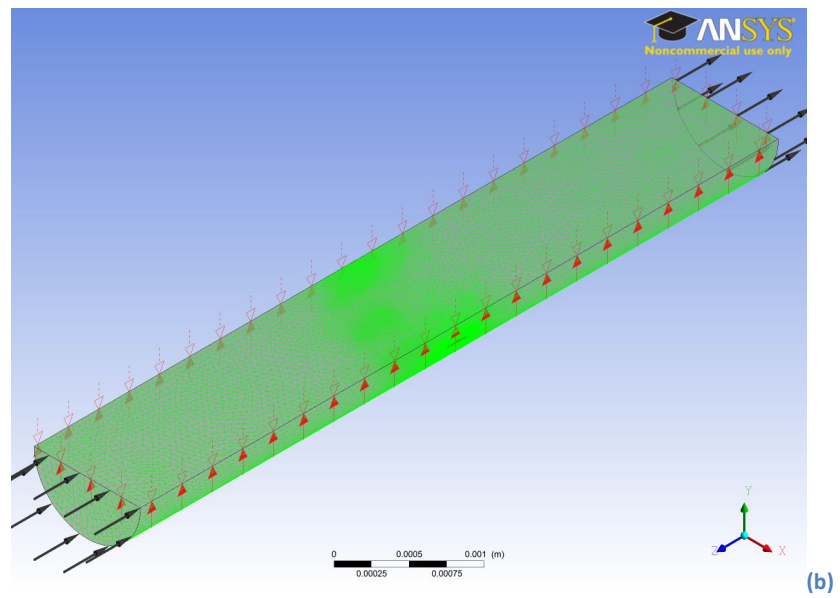
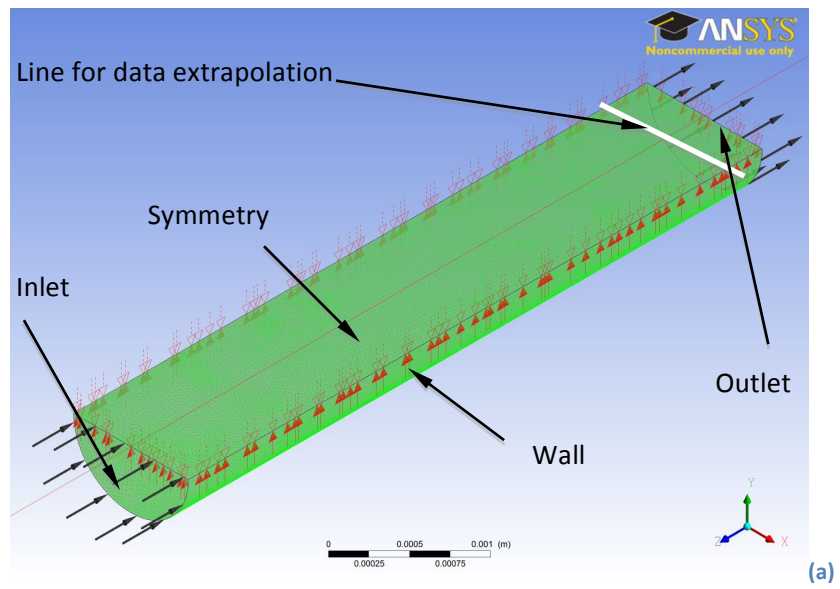


Figure 3.8 - ANSYS-CFX (a) pristine, (b) sutured and (c) coupled blood vessel models, inc. boundary conditions

Benchmarking

All benchmarking studies were carried out using water as the working fluid. A laminar solution was sought as the Reynolds number (1.1) was low, i.e. $90 \ll 2300$ - the accepted duct flow transition value (19). This benchmarking process was performed to establish computationally the length of duct required for the flow to become fully developed, which is known (101) to be larger than observed experimentally (in this case $0.06 Re_d d \sim 6d$ (19); where a paraboloid velocity distribution is expected (Figure 3.9).

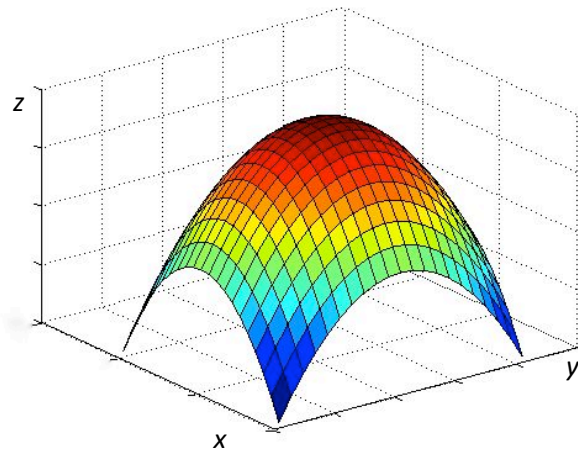


Figure 3.9 - Paraboloid velocity distribution in a straight rigid circular vessel with constant flow (created in MathWorks MATLAB)

The benchmarking routine applied a mass flow rate of $1.045 \times 10^{-4} \text{ kg s}^{-1}$ (calculated from the maximum arterial flow from (40)) at the inlet through a circular duct of 1 mm diameter that is analogous to the blood vessels to be investigated. Data from these analyses are shown in Figure 3.10. Here, the open circles represent the velocity values extrapolated from a diameter toward the outlet of the model as indicated in Figure 3.8(a). The crosses signify velocity data values obtained from an analogous diameter approximately at the models centre. These data clearly show the development of the flow field. The theoretical solution of the Navier-Stokes equations is also denoted in Figure 3.10 as the continuous line.

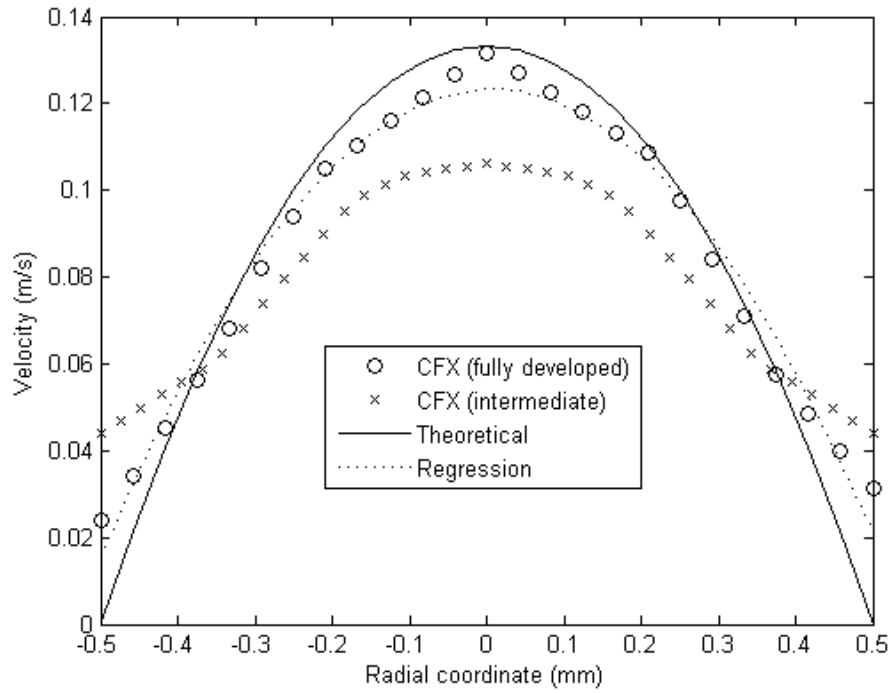


Figure 3.10 - Comparison of theoretical and analytical velocity profiles

The data show the velocity field is a function of only the radial coordinate in these special cases. Hence, as suggested previously, an analytical theoretical model could be developed for this pristine case from direct solution of the Navier-Stokes equations (2.5), transformed into cylindrical coordinates and neglecting the hoop and axial momentum terms, as follows:

$$\rho \frac{dV}{dt} = \rho g - \frac{dp}{dz} + \mu \frac{1}{r} \frac{\partial}{\partial r} \left(r \frac{\partial v}{\partial r} \right)$$

(3.1)

Since the fluid was modelled horizontally under steady state conditions the first two terms vanished and equation (3.1) became:

$$\frac{dp}{dz} = \mu \frac{1}{r} \frac{\partial}{\partial r} \left(r \frac{\partial v}{\partial r} \right)$$

The physics dictated that the term on the left hand side was constant, as a constant pressure drop must drive the flow:

$$\frac{\Delta p}{L} = \mu \frac{1}{r} \frac{d}{dr} \left(r \frac{dv}{dr} \right)$$

where L was the length of the duct. Noting here, the change to ordinary differentials as opposed to partial differentials since the data indicated that the velocity field was solely a function of the radial coordinate, therefore:

$$\frac{\Delta p}{\mu L} r = \frac{d}{dr} \left(r \frac{dv}{dr} \right)$$

Integrating twice rendered:

$$v(r) = \frac{\Delta p r^2}{4\mu L} + c_1 \ln(r) + c_2$$

(3.2)

where c_1 and c_2 were the constants of integration. The first constant of integration must be zero as the velocity was singularly defined and bounded (i.e. not minus infinity) at this point i.e. 0.13 m s^{-1} in this particular case (Figure 3.10). Moreover, the non-slip boundary condition implied that velocity must be zero at the walls, i.e. when $r = R$, therefore:

$$v(r) = -\frac{R^2 \Delta p}{4\mu L} \left(1 - \frac{r^2}{R^2} \right)$$

(3.3)

It was this function that was plotted as the theoretical curve in Figure 3.10 for comparison with the CFD data obtained from the ANSYS CFX commercial code.

In addition, a second order (quadratic) fit of the CFD data obtained from the end of the model was included as a dotted line for further comparative purposes. This implies that the ANSYS

CFX software calculated an accurate velocity distribution in both undeveloped and developed flow forms. This was evidenced by the data obtained from the centre of the model lying under the data obtained towards the outlet of the model, thus indicating underdeveloped flow closer to the inlet, as expected. Particularly good agreement was shown between the data obtained from the end of the model and the analytical model derived in this section (equation (3.3)). Further incontrovertible evidence of a quadratic velocity distribution was obtained by observing the least-squared fit of these particular data. Incidentally, the correlation coefficient between the theoretical and least-square fit data was 0.999, which strongly indicates that the CFD data obtained and the theoretical model developed here describe an identical physical phenomenon.

It should be noted that these results were obtained from models approximately 30 mm in length to enable the flow to fully develop. Since the vessels to be simulated were part of a larger cardiovascular system, a pertinent assumption therefore was that flow through the anastomosed vessels would be fully developed. Hence, all steady state simulations that followed applied a paraboloid velocity profile to the inlet using functionality within the ANSYS-CFX software. This well-recognised technique has been demonstrated in previous work (48,76). In a straight vessel, fluid moves at different velocities at different points, with fast flow in the centre and slow flow at the walls. This pattern is a result of friction between the fluid and the vessel wall and within the fluid itself, and it assumes a parabolic profile (102). In Rickard's (40) study, the aforementioned assumption of a paraboloid velocity distribution was imposed on all models, that is, the following expression was applied at the inlet:

$$v(r) = -\frac{2Q}{\pi R^2} \left(1 - \frac{r^2}{R^2}\right)$$

(3.4)

where Q is the volumetric flow rate. This expression was made equivalent to the analytical model developed earlier in this section by integration of equation (3.3), rendering the volumetric flow rate:

$$Q = \frac{\pi R^4 \Delta p}{8\mu L}$$

and substituting the pressure drop per unit length into equation (3.3). Incidentally, the ANSYS-CFX software required a mass flow rate ($\dot{m} = \rho Q$) in order to define velocity distribution.

Hence, this definition was substituted into equation (3.4) to give:

$$v(r) = \frac{2\dot{m}}{\pi\rho R^2} \left(1 - \frac{r^2}{R^2}\right)$$

(3.5)

It was this equation that was applied in the software at the inlet for all steady state simulations.

Steady state vessel models

All steady state vascular simulations were carried out using blood as the working fluid. This was modelled as an incompressible Newtonian fluid with a density of 1060 kg m^{-3} and dynamic viscosity of 0.0035 Pa s in accordance with current literature (40,45,63,75,76).

All simulations were conducted using the laminar flow model, as the Reynolds number (Re, equation (1.1)) for these models was low ($\text{Re} \approx 90$).

All arterial models were given a constant mass flow rate of $1.045 \times 10^{-4} \text{ kg s}^{-1}$; this was calculated from the maximum volume flow rate through the right femoral artery of a single 410 g outbred male Wistar rat in the study by Rickard *et al.* (40). A summary of all data entered into the simulations can be found in Table 4.1.

3.3.2 Outlet

All simulations were conducted with identical outlet conditions. The relative pressure was set to zero in all models so as not to influence the flow phenomena or recirculation patterns upstream. This method was previously used on clinically relevant models (40). The location of the outlet boundary is demonstrated in Figure 3.8(a).

3.3.3 Wall

In keeping with previous studies (40,63,73,76,82), including an international study on intracerebral blood flow (75), all walls were simulated as rigid, non-compliant structures with non-slip conditions. As such, the boundary condition applied to all walls was that of zero velocity and hence maximum shear stress. The wall boundary can be seen in Figure 3.8(a).

3.3.4 Symmetry

All models were created with a symmetry condition axially in the longitudinal plane, as demonstrated in Figure 3.8(a). This method has also been employed in similar research on blood flow modelling (40).

3.4 Post-processing

All simulations were examined using the high-end graphical post-processing software ANSYS CFD-Post. This programme was the common post-processor to the ANSYS fluid dynamics family of products and enabled clear analysis and visualisation of results.

ANSYS CFD-Post had a wide range of features including mesh visualisation, the ability to define locations for quantitative calculations, and a graphical user interface with a viewer pane to display the generated outputs (103).

There are a variety of methods available to provide visual representations of the calculated data, which can be extremely beneficial to gain an overall impression of the data at a glance. Fluid flow can be represented as streamlines, vector plots, or vortex cores, as well as many other methods, and all can be animated using the movie function.

As well as producing visual displays of the flow data, the post-processor permits powerful quantitative data analysis. It is possible to create charts of variables such as velocity, pressure, and WSS at any given point, or surface, on the geometry. These can be tabulated as a dataset and incorporated into a report containing all the generated images, charts and movies for presentation purposes or further statistical analysis.

All simulations in this study underwent a basic set of post-processing interventions to produce the data for analysis, although some models required further, more detailed processing. Each model was analysed to demonstrate the velocity and pressure profiles throughout. Wall velocity (boundary layer velocity) and wall-pressure profiles were also created for each geometry, to examine the flow in this region in more detail. Velocity streamlines were generated from the inlet and animated to better visualise the overall flow pattern, and vortex cores were produced to demonstrate the vorticity caused by the variance in geometry, particularly at the wall in the anastomotic region. Vorticity is defined as the curl of the velocity field and as such might indicate regions of recirculating flow, and subsequently areas of potential clot development. Importantly, as high WSS had been linked to platelet activation and therefore thrombus formation, WSS and SSR were also determined for each simulation.

Images demonstrating the output of each stage of the post-processing phase are shown subsequently in the figures of Chapter 4.

3.5 Statistical analysis

The CFD software generated a large quantity of data, and as such, only directly applicable data were statistically analysed. In particular, the values for WSS underwent initial analysis using a Lillie test to ensure a normal distribution, and subsequently, a one-tailed Student's t-test was performed. A one-tailed Student's t-test was used as it was clear from the data that there was a difference in the WSS in one direction only i.e. an increase, and for this reason, a two-tailed t-test would be unnecessary (104).

Results with p values $< 0.1\%$ (0.001) were deemed significant. The data were assumed to be homoscedastic in nature, and this was confirmed using Fisher's test. Discussion of the statistical analysis is found in sections 4.2 and 5.2. Where possible, data are presented as mean \pm Standard Error of the Mean (SEM $\pm 10\%$).

4 Results

This chapter presents the results obtained from all vessel simulations performed in this research. Input data for the simulations are displayed below in Table 4.1.

Vessel diameter	1 mm
Vessel section length	5 mm
Vessel walls	Non-compliant, Non-slip
Flow regimen	Laminar, Steady-state
Reynolds number (Re)	≈90
Fluid type	Blood (Newtonian)
Blood density	1060 kgm ⁻³
Blood viscosity	0.0035 Pa s
Inlet profile	Paraboloid (fully developed flow)
Mass flow rate	1.045x10 ⁻⁴ kg s ⁻¹ (Calculated from (40))
Relative pressure	0 Pa
Advection scheme	High resolution (ANSYS default)
Convergence control	1-100 iterations (ANSYS default)
Convergence criteria Root Mean Squared (RMS)	1x10 ⁴ (ANSYS default)

Table 4.1 - Summary of input data parameters

4.1 Vessel simulations

The results for the vessel simulations are presented below. Evaluation of velocity profiles, pressure contours, WSS, SSR and vorticity distributions are addressed in turn for each of the pristine, sutured and coupled anastomoses.

4.1.1 Velocity profiles

The results obtained for the primary velocity field are shown in Figure 4.1.

Pristine

The velocity distribution being shown in Figure 4.1(a) where a zero velocity is observed as expected at the walls of the pristine vessel; the maximum velocity $\sim 0.25 \text{ ms}^{-1}$ being evaluated at the central core which is in complete agreement with application of equation (3.5), with the appropriate variables set as in section 3.3.1. Furthermore, it can be seen that the profile is unchanged throughout the length of the vessel signifying the steady-state solution (equation (3.5)). This is expected, since there are no changes in the geometry and, as mentioned previously, a laminar solution was sought.

Further evidence of adherence of the CFD solution to the analytical model developed in section 3.3.1 is shown in Figure 4.1(b). Here, the *wall velocity*¹³ is shown and ranges from 4.2×10^{-5} to $8.5 \times 10^{-3} \text{ ms}^{-1}$ which are over two orders of magnitude less than the applied maximum velocity, indicating a near-zero velocity at the wall. However, these values show a divergence from the wall velocity boundary condition (which should of course be zero). This can be interpreted as a plot of the *boundary layer velocity* profile where a significant jump totalling two orders of magnitude is observed at a distance of approximately 0.02 mm from the wall. Interestingly, this boundary layer velocity profile gives not only a qualitative but also a quantitative measurement of boundary layer flow in all types of vessels investigated throughout this work. That is, values higher than the maximum velocity indicated in Figure 4.1(b) signify accelerated flow due to geometrical changes; conversely, decelerated or sluggish flow within the boundary layer can also be demonstrated.

The CFD data presented are in remarkably good agreement with equation (3.5) and therefore Figure 3.10. From the analysis performed, it can consequently be inferred that the pristine vessel model is in excellent agreement with theory and as such is physically realistic.

¹³ As defined by the ANSYS CFX software

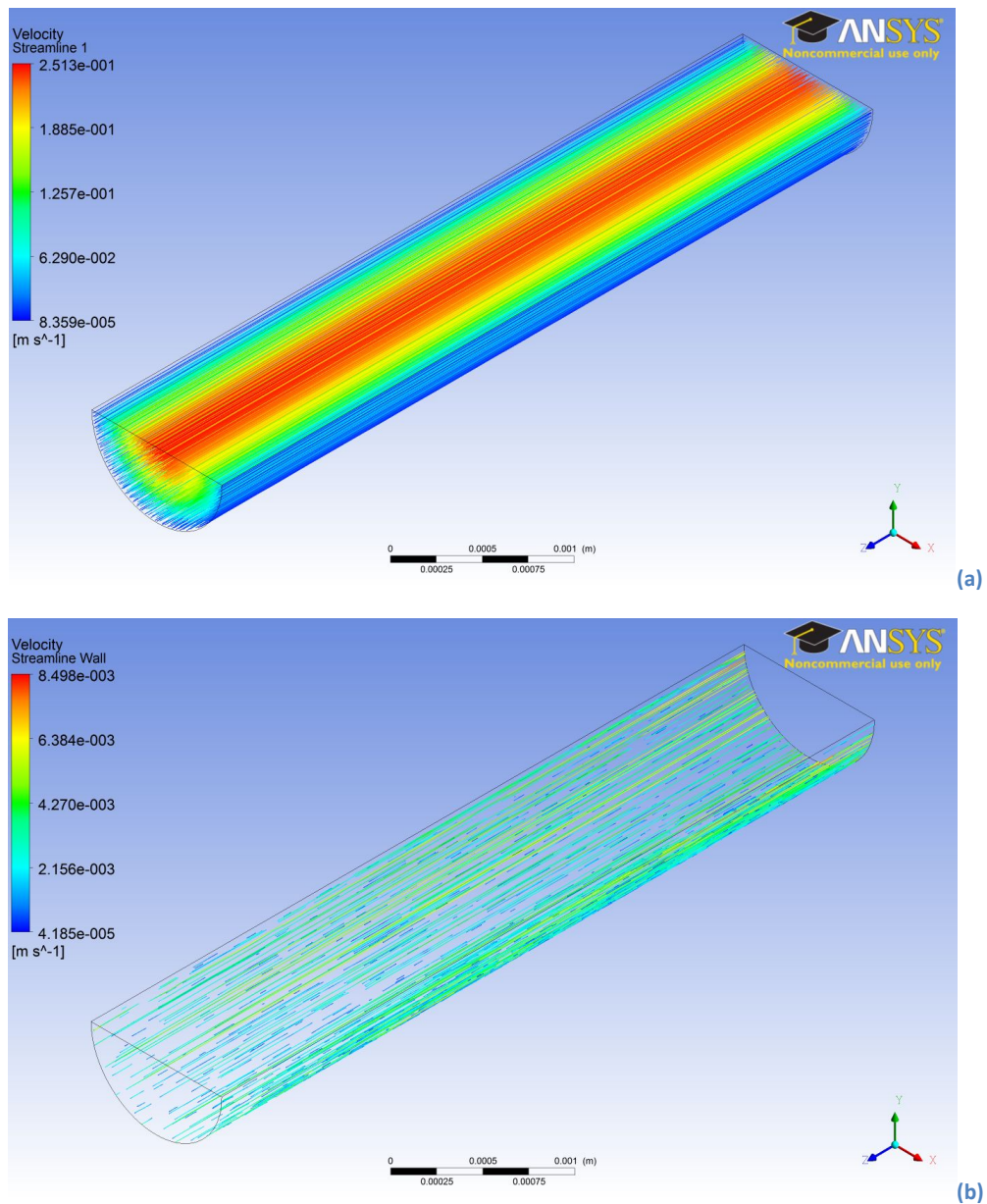


Figure 4.1 - Pristine CFX streamlines (a) velocity profile, (b) boundary layer velocity profile

Sutured

The velocity profiles for the sutured anastomosis are shown in Figure 4.2. The complete velocity field is demonstrated in Figure 4.2(a) with a maximum velocity of $\sim 0.25 \text{ ms}^{-1}$ being observed in the central core region which is almost identical to that of the pristine model, as expected. The profile remains largely unchanged throughout its length, however, there is altered flow around the sutures which can be seen in Figure 4.2(b) and (c). These images show fluid diverging around the suture material and slowing.

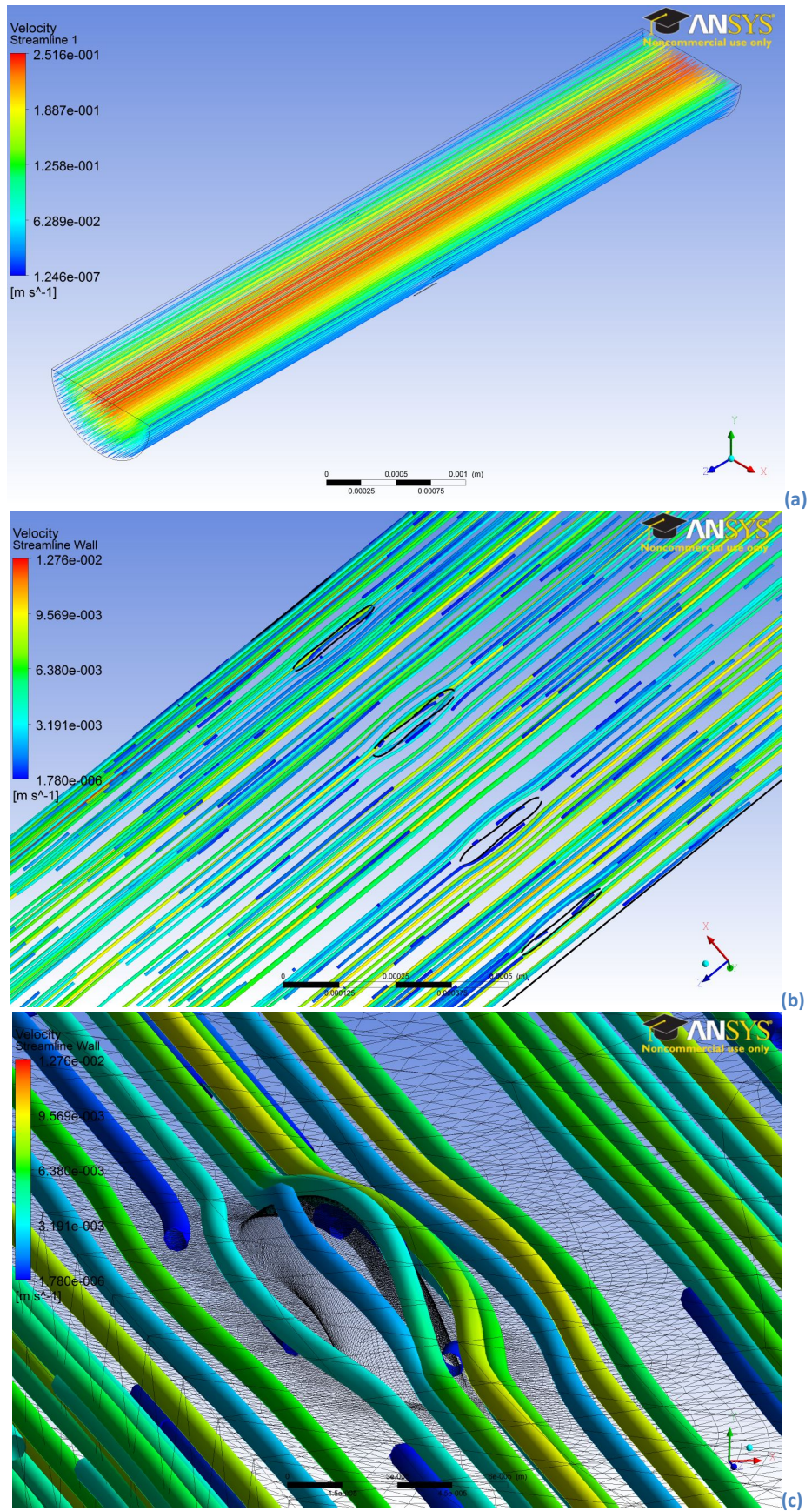


Figure 4.2 - Sutured CFX streamlines (a) velocity profile, (b) boundary layer velocity profile and (c) close up of single suture boundary layer velocity profile with underlying mesh

Coupled

The coupled anastomosis velocity profiles are shown in Figure 4.3(a) to (c). The complete velocity field is demonstrated in Figure 4.3(a) again, unsurprisingly, a maximum velocity of $\sim 0.25 \text{ ms}^{-1}$ is observed in the central region which is almost identical to that of the pristine and sutured models. Again, the profile remains largely unchanged throughout its length; however, there is some altered flow in the anastomotic region which can be seen in Figure 4.3(b) and (c). Fluid is shown deviating around the reflected vessel wall. Analysis of the absolute figures for both sutured and coupled velocity profiles reveals remarkably similar results for these techniques. Direct comparison of the average and maximum velocities for each vessel simulation can be seen in Table 4.2, with the sutured and coupled models producing almost identical values.

	Mean boundary velocity ($\times 10^{-3} \text{ ms}^{-1}$)	Maximum boundary velocity ($\times 10^{-3} \text{ ms}^{-1}$)
Pristine	4.33 \pm 0.2	6.43 \pm 0.3
Sutured	6.32 \pm 0.3	9.62 \pm 0.5
Coupled	6.24 \pm 0.3	9.34 \pm 0.5

Table 4.2 - Mean and maximum boundary velocity comparison inc. SEM depicted as ANSYS default of 10%

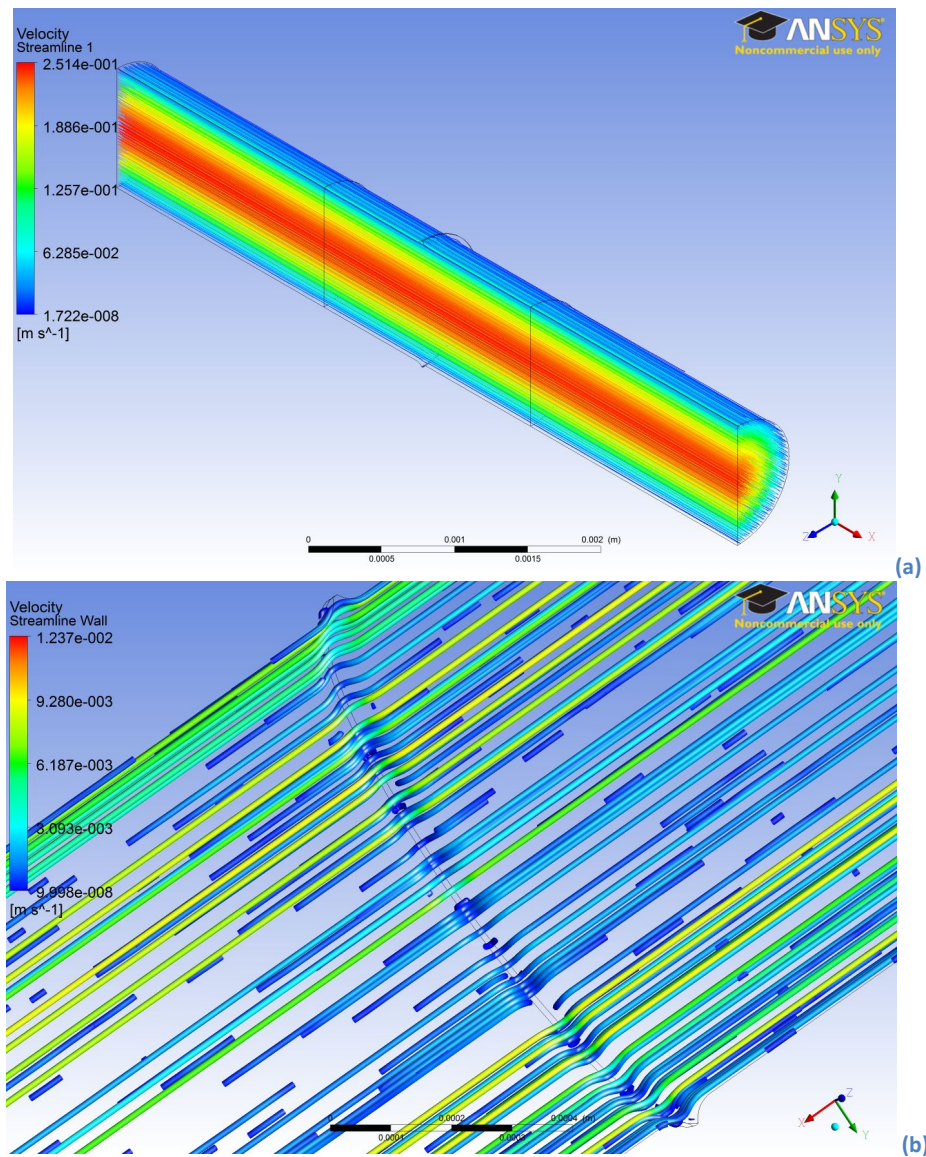


Figure 4.3 - Coupled CFX streamlines (a) velocity profile, (b) internal boundary layer velocity profile

4.1.2 Pressure contours

The resulting pressure contours as calculated from the velocity distribution (Figure 4.1), are shown in

Figure 4.4(a) and (b) on the symmetry plane and at the wall respectively; which are approximately equal within numerical convergence. These demonstrate a linear pressure drop from the inlet to the outlet, which is certainly the case physically. This is a consequence of the velocity distribution remaining unchanged throughout the vessel (steady-state with no geometrical changes) and a relative static pressure of zero being applied at the outlet,

meaning the pressure is driving the flow in this and all subsequent cases. Furthermore, the value of the pressure drop can be verified via combination of equations (3.3) and (3.5), followed by integration with respect to the z-coordinate, thus:

$$p(z) = \frac{8\mu\dot{m}(L - z)}{\pi\rho R^4}$$

(4.1)

Application of this equation gives a value of pressure drop of 70.3Pa over the full length of the vessel, which implies that the derived CFD pressure values are less than 5% in error when compared to this exact theoretical value. This error is acceptable since the convergence sought during the solution of the CFD model was set to the default value of 10% in the ANSYS-CFX software.

A further, more rigorous, comparison between the CFD data obtained from a line located through the centre of the vessel on the symmetry plane and values calculated from the theoretical analytical model are shown in Figure 4.5, where excellent agreement is demonstrated. Regression analysis of these data with analytically calculated data reveals a perfectly correlated linear regression coefficient of 1.02. Since the underlining physics and modelling assumptions for both techniques are identical, this demonstrates that both the analytical and CFD data are modelling an identical phenomenon of blood flow through a pristine vessel.

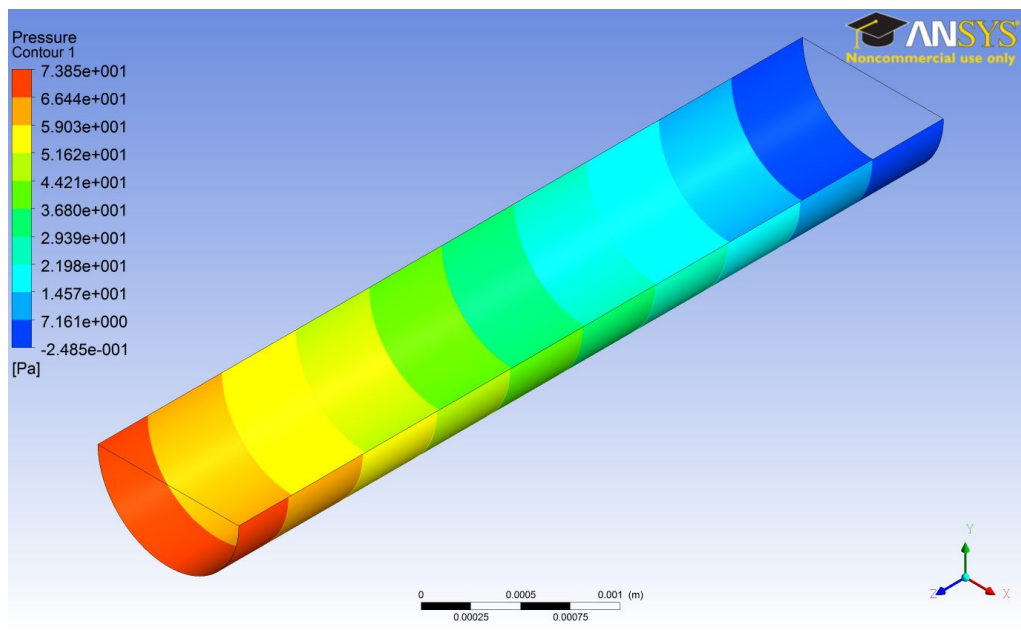
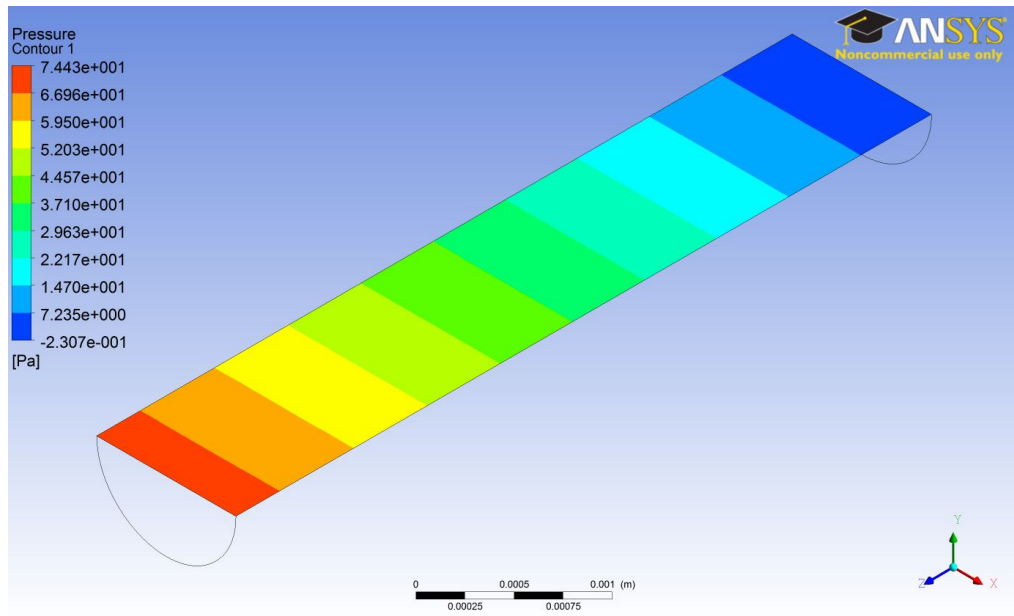


Figure 4.4 - Pristine CFX pressure contours at (a) symmetry plane and (b) wall

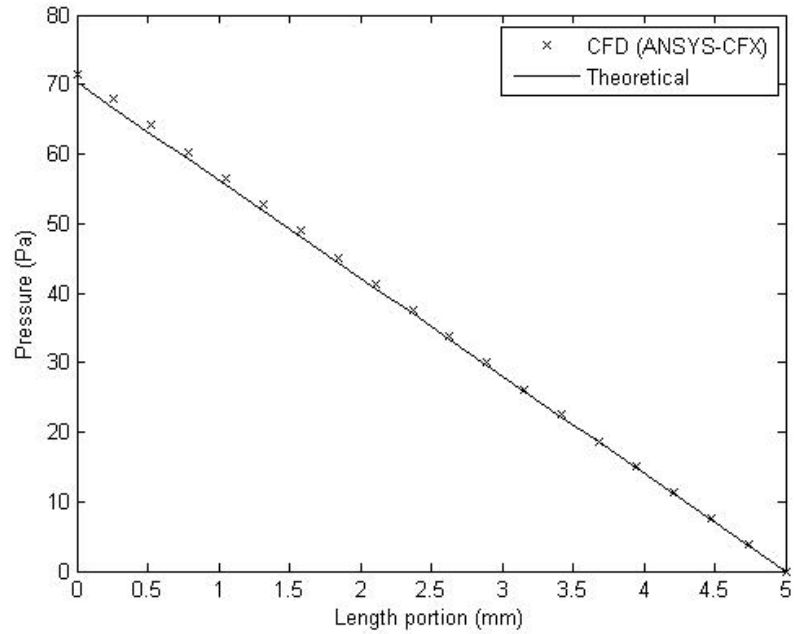


Figure 4.5 - Pristine CFD and theoretical pressure profile comparisons

Pressure contours for the sutured anastomosis are shown at both the symmetry plane and the wall in Figure 4.6(a) and (b). There is an overall linear pressure drop from the inlet along the vessel length that is comparable to that of the pristine model. However, the inlet pressure in this simulation is 88 Pa, which is higher than that of the pristine model (74 Pa) indicating restriction in the flow field due to the change in geometry. Hence, a higher pressure is required to maintain the flow rate. The addition of the suture material has altered the pressure profile at the walls, more specifically, at the site of the sutures themselves. Here, an increased pressure is seen on the proximal *upstream* edge of the suture, with a relatively low pressure demonstrated distally as expected.

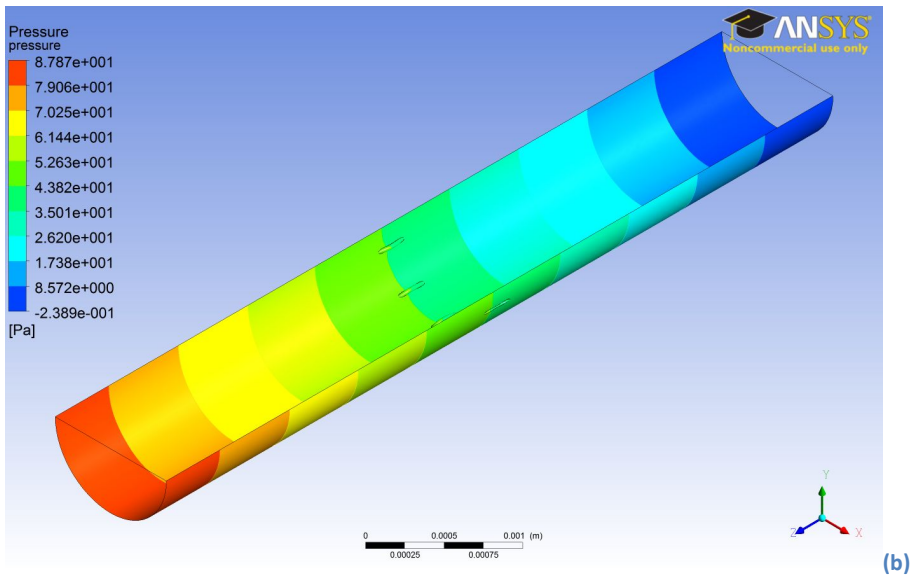
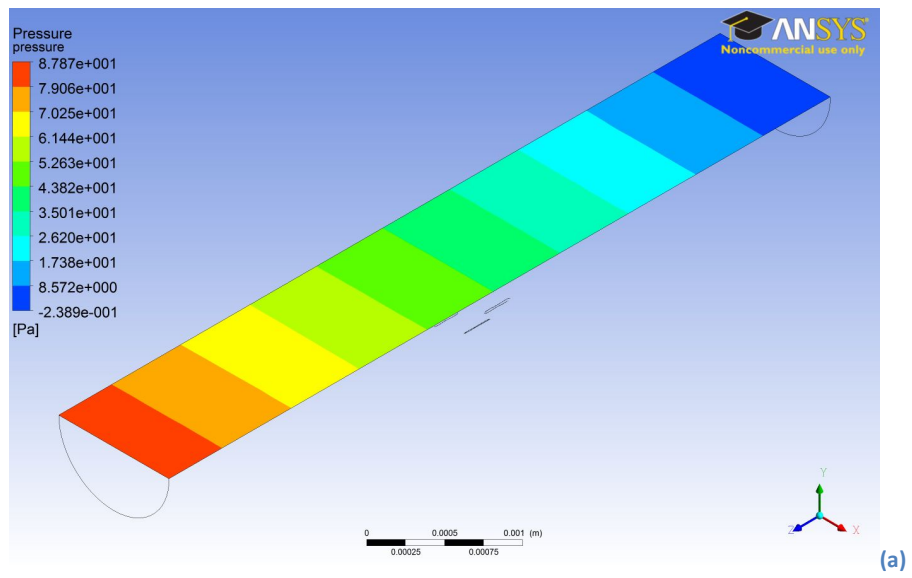


Figure 4.6 - Sutured CFX pressure contours at (a) symmetry plane and (b) wall

Pressure contours for the coupled anastomosis are demonstrated at both the symmetry plane and the wall in Figure 4.7(a) and (b). Again, there is an overall linear pressure drop from the inlet along the vessel length, which is comparable to that of both the pristine and sutured models. As expected, a reduced pressure is seen on the proximal *upstream* edge of the annular region, with a relatively higher pressure demonstrated distally.

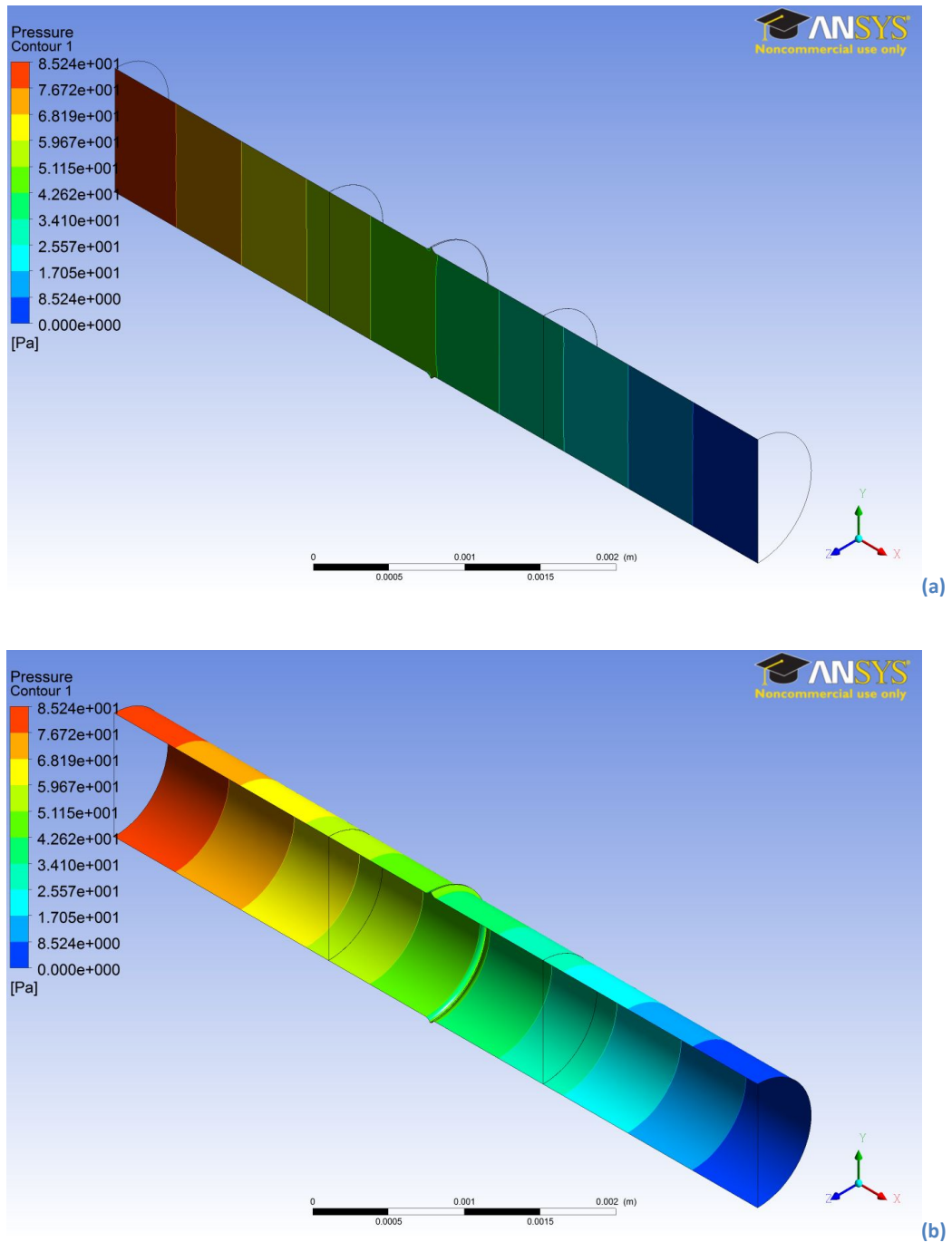


Figure 4.7 - Coupled CFX pressure contours at (a) symmetry plane and (b) wall

4.1.3 Wall Shear Stress (WSS) and Shear Strain Rate (SSR)

Since it is known from the literature that changes in the WSS can lead to platelet activation and subsequently thrombus formation (93,94), then it is important to consider such data from the CFD code (Figure 4.8), where an average value of approximately 3.5 Pa is observed, if the Saint-Venant's (105) edge effects are neglected. Moreover, for pristine vessels, analytical values can be obtained and serve as a final validation of methods. Hence the average value shown can be compared with the analytical model developed previously via differentiation of the velocity field (3.5), thus:

$$\tau(R) = \frac{4\mu\dot{m}}{\pi\rho R^3}$$

(4.2)

Where $\tau(R)$ is the shear stress when $r = R$, that is the wall shear stress. Application of this renders a value of 3.51 Pa for the fluid simulated as in Figure 4.8; hence further demonstrating excellent agreement between the CFD modelling data and the theoretical solution of the Navier-Stokes equations (section 3.3.1).

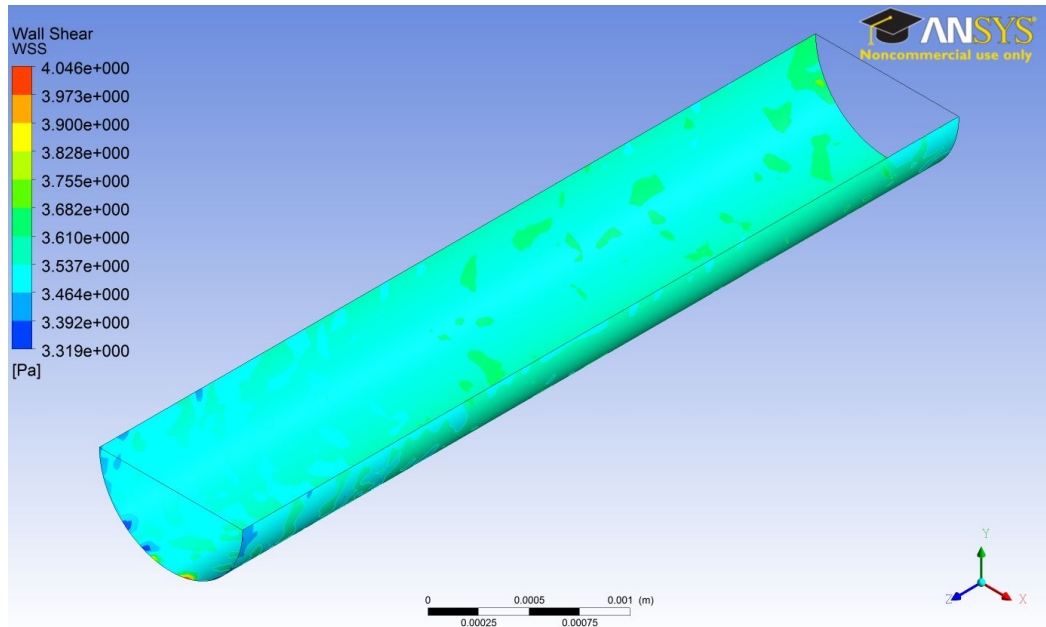


Figure 4.8 - Pristine CFX wall shear stress contour

Profiles created for the WSS in the sutured model are shown in Figure 4.9(a) to (c). Like the pristine model, the distribution is even throughout the vessel, however, the average WSS is 4.54 Pa with a maximum WSS of 9.91 Pa. This is considerably larger than that of the pristine model, where the average WSS is 3.50 Pa and the maximum is 3.82 Pa. A direct comparison of the WSS in all three models can be seen in Table 4.3. Although the average WSS is larger and relatively uniform throughout the vessel, most importantly the areas of highest WSS are the suture sites themselves, see Figure 4.9(b) and (c). In terms of thrombogenic potential, these isolated areas of high WSS are a significant finding.

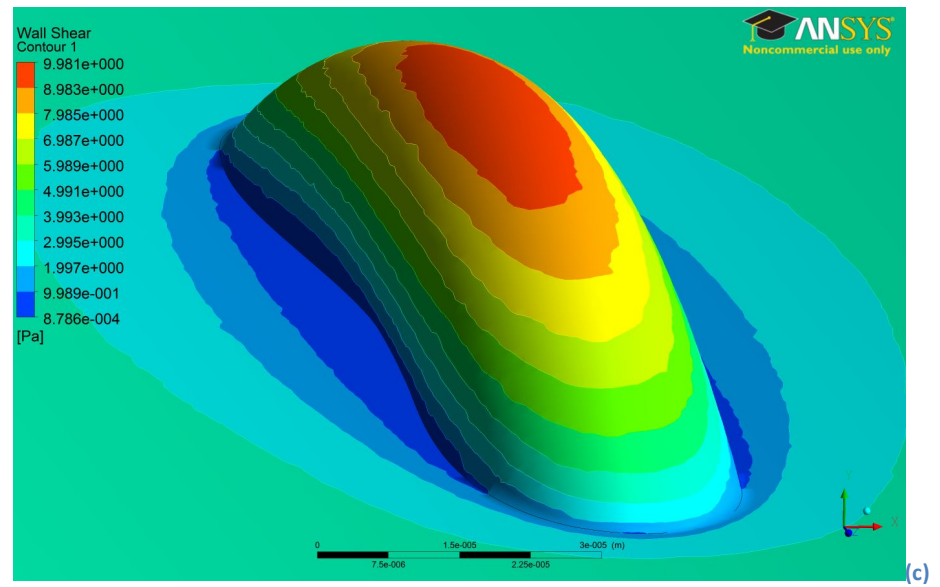
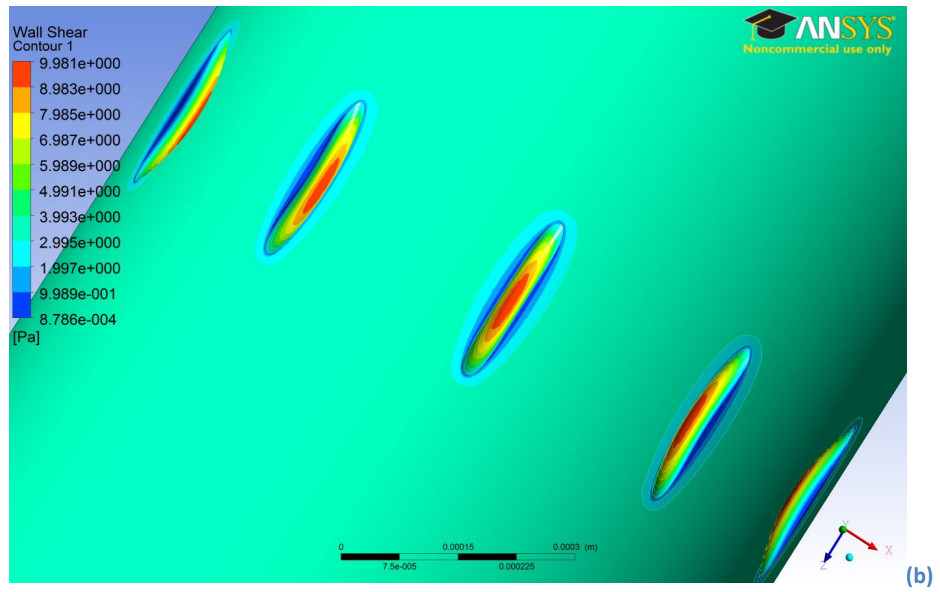
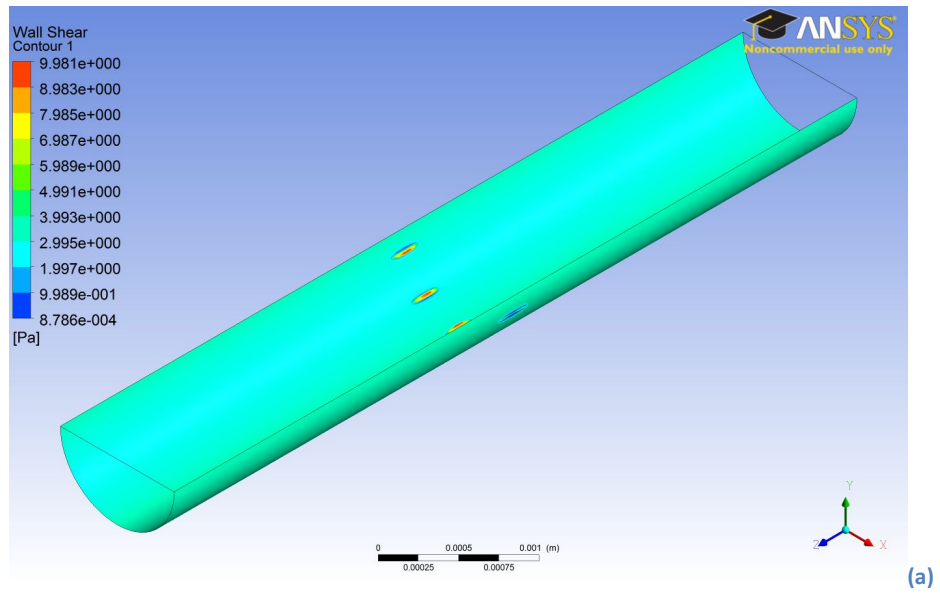


Figure 4.9 - Sutured CFX wall shear stress contour at (a) whole vessel, (b) anastomosis and (c) close up of single suture

The Shear Strain Rate (SSR) for the sutured anastomosis is plotted below in Figure 4.10. As SSR is proportional to WSS in Newtonian fluids, the profile for SSR is unsurprisingly similar to that of the WSS. It is clear to see that the maximum SSR (approximately $2.70 \times 10^3 \text{ s}^{-1}$) is present at the suture sites, which is well above the threshold of $1 \times 10^3 \text{ s}^{-1}$ (93,94) where platelets become activated and blood coagulation is precipitated. The average SSR is approximately $0.80 \times 10^3 \text{ s}^{-1}$.

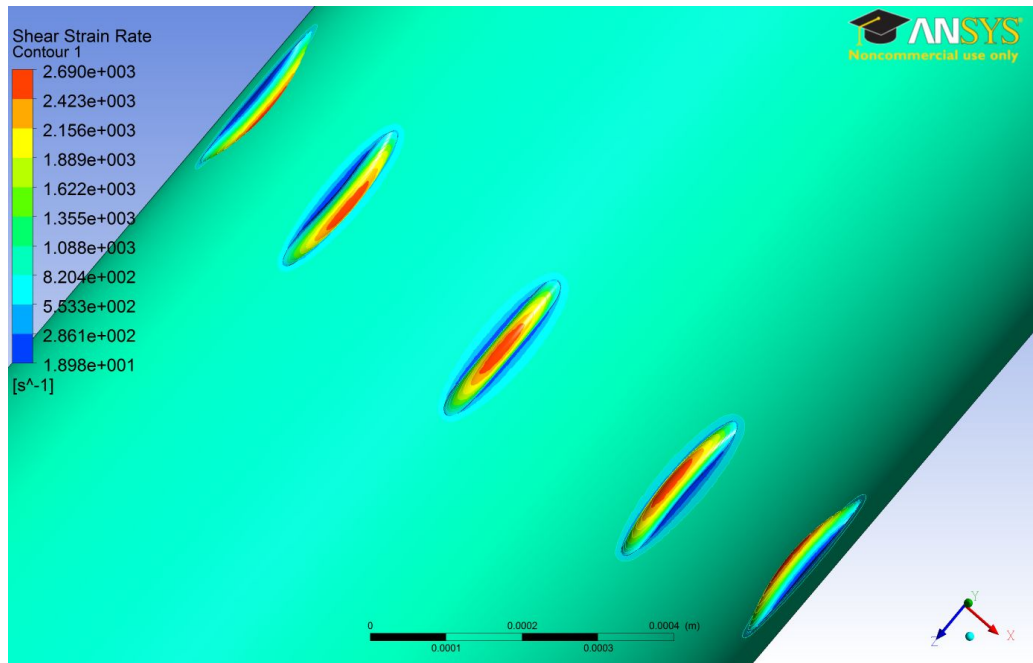


Figure 4.10 - Sutured CFX shear strain rate at the anastomosis site

WSS profiles for the coupled model are shown in Figure 4.11(a) and (b). As with both the pristine and sutured models, the overall distribution is even throughout the vessel. The average WSS in this case was 3.52 Pa with a maximum WSS of 4.82 Pa. These figures are almost identical to those of the pristine model, where the average WSS was 3.50 Pa and the maximum 3.82 Pa, indicating that the coupler does not drastically alter the WSS. A direct comparison of the WSS in all three models can be seen in Table 4.3, which clearly shows that both the average and maximum WSS is notably higher in the sutured simulation. The distribution of the WSS at the coupled anastomosis site (Figure 4.11(b)) is regular and circumferential.

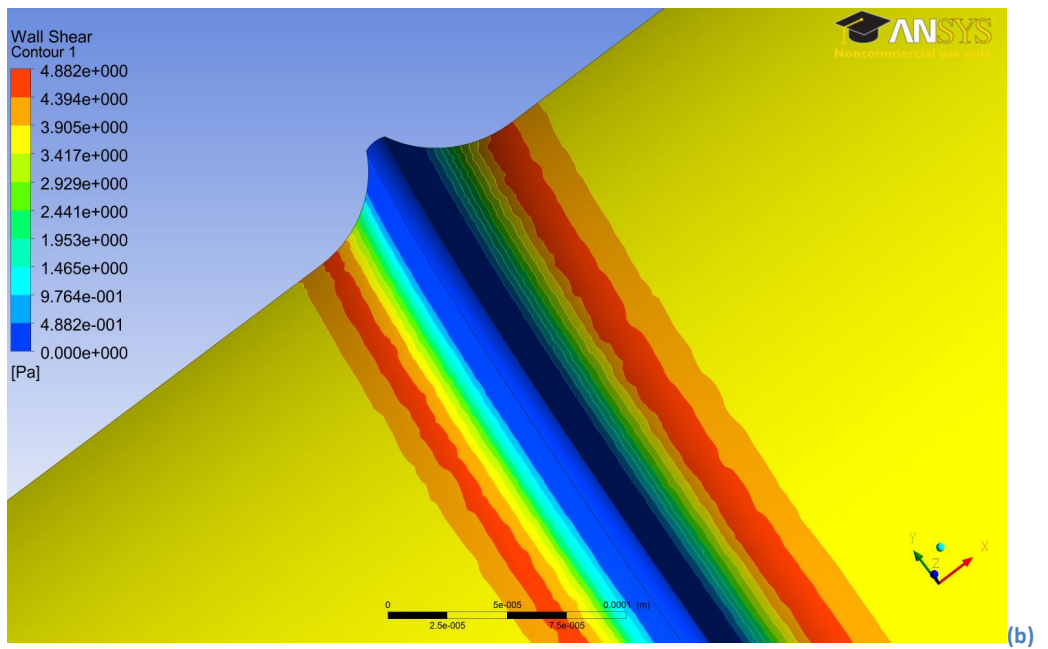
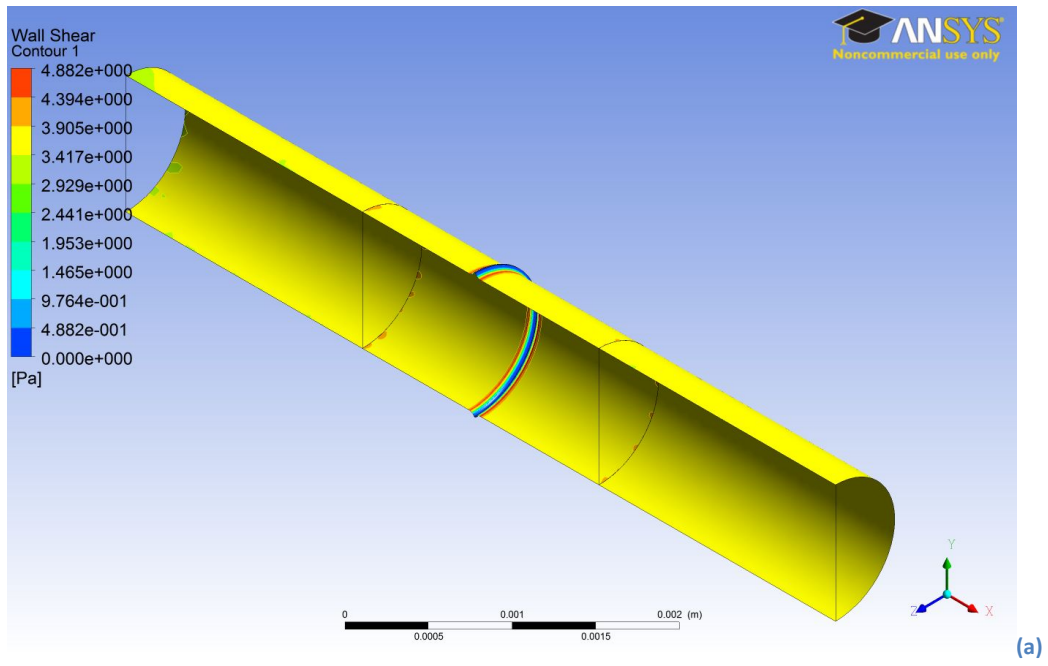


Figure 4.11 - Coupled CFX wall shear stress contour at (a) whole vessel and (b) close up of coupler site

	Mean wall shear stress (Pa)	Maximum wall shear stress (Pa)
Pristine (CFD)	3.50 ± 0.17	3.82 ± 0.2
Pristine (Analytical)	3.51 ± 0.0	3.51 ± 0.0
Sutured	4.54 ± 0.2	9.91 ± 0.5
Coupled	3.52 ± 0.17	4.82 ± 0.2

Table 4.3 – Mean and maximum wall shear stress comparison inc. SEM depicted as ANSYS default of 10%

The coupled anastomosis SSR contour is plotted below in Figure 4.12. Again, the profile for SSR is unsurprisingly similar to that of the WSS. The maximum SSR is present in a thin annular region and measures approximately $1.25 \times 10^3 \text{ s}^{-1}$, which is just above the threshold of $1 \times 10^3 \text{ s}^{-1}$ (93,94) where platelets become activated and blood clotting initiated. Despite this, the value is less than half the maximum SSR seen at the suture sites in the sutured simulation; the average SSR however, remains comparable and is approximately $0.85 \times 10^3 \text{ s}^{-1}$.

Based on the assumption¹⁴ that higher SSRs are proportional to the amount of platelet activation, this indicates that the higher the SSR, the greater proportion of platelets will be activated, thereby increasing the amount and rate of thrombus formation.

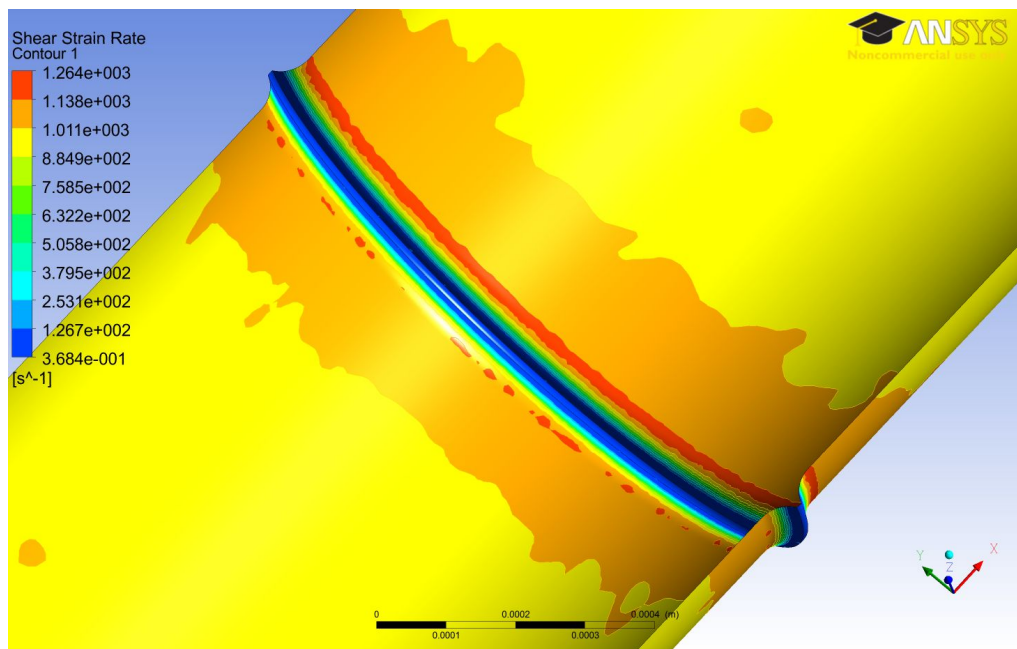


Figure 4.12 - Coupled CFX shear strain rate at the anastomosis site

¹⁴ As platelets become activated and form aggregates, the hydraulic diameter of the system (r in equation (4.1)) reduces, thereby increasing pressure at the anastomotic site (106). This pressure increase is resolved into the shear stress at the walls, which is proportional to the SSR.

4.1.4 Vorticity

A further potential indicator for the formation of blood clots within a vessel is disrupted flow. This can in part be demonstrated by measurement of recirculation patterns within the fluid domain, in the form of vortices. From a fluid dynamics viewpoint, the formation of vortices can be determined from the vorticity¹⁵ of the flow, which is defined as the curl of the velocity field. In physical terms this represents the angular velocity relative to the principal axes, that is to say the amount of rotation of the flow around these axes. It should be noted that vorticity may be present whether the flow is laminar or turbulent. Indeed, for the blood flow examined in all models here, vorticity is not only present but quite significant. This is due to the radius of the vessels being particularly small. It can be demonstrated directly from recourse to the definition where $2\omega = \frac{2u(0)}{R} = \frac{2 \times 0.25}{0.0005} = 1,000 \text{ rad s}^{-1}$ (see Figure 4.13). It should be pointed out that this large vorticity effect is present at the *wall* where the velocity gradient is greatest, and acts at right angles to the velocity flow field.

To gain an understanding of probable locations of recirculating blood flow, calculations were obtained of the vorticity greater than that which would occur naturally in the pristine vessel. In the pristine simulation, the proportion of vorticity equal to or greater than $1,000 \text{ rad s}^{-1}$ is negligible. This serves as a natural benchmark for comparison with the analogous sutured and coupled models.

¹⁵ An excellent explanation and demonstration of this physical phenomenon is given by Prof. A. Shapiro in a 1961 educational film produced by the MIT (www.youtube.com/watch?v=loCLkcYEWD4)

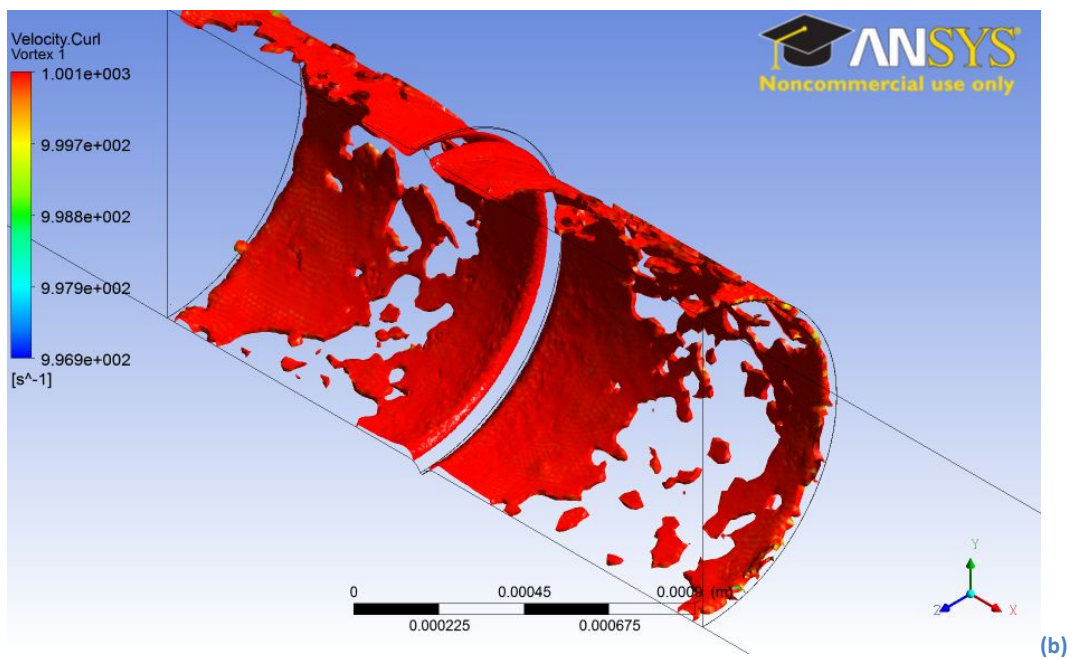
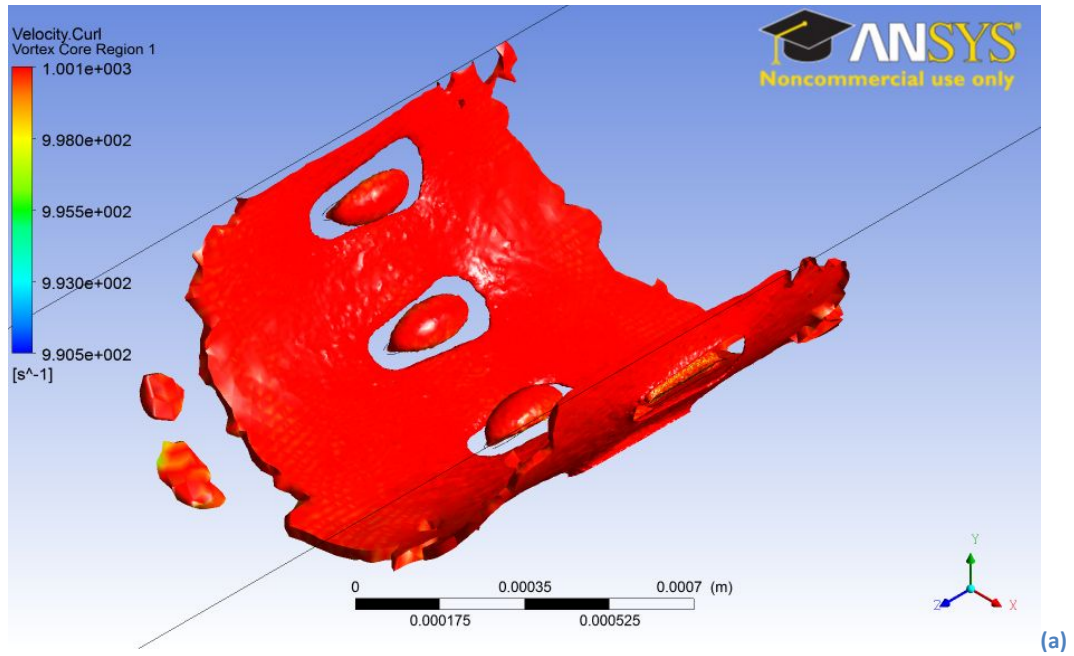


Figure 4.13 - Vorticity profiles for (a) sutured and (b) coupled simulations

Figure 4.13 illustrates the boundary layer vorticity profiles in the sutured (a) and coupled (b) anastomoses, respectively. Vorticity values exceeding those that occur naturally i.e. 1,000 rad s⁻¹ are shown in red, and from a qualitative perspective there is a greater vorticity density at the sutured anastomosis, particularly at the suture sites, than the coupled anastomosis. The

coupled vorticity profile does not demonstrate any vorticity at the actual anastomotic site and the distribution around the anastomosis is more scattered and less concentrated.

4.2 Statistical analysis

As mentioned in section 2.5, high WSS and SSR are related to platelet activation and hence thrombus formation. This implies that, in order to decipher the relative likelihood of blood clot propagation as a result of the surgical procedure, the WSS of the sutured and coupled anastomoses should be as close to that of the pristine (natural) case as possible. Hence, the regions of highest WSS within the models indicate the most likely locations for thrombus formation. It is therefore necessary to determine whether the WSS values for the sutured technique are significantly greater than those for the coupled method as suggested in Table 4.3. From a statistical analysis viewpoint, this statement can be expressed as the null (H_0) and scientific (H_s) hypothesis respectively, thus:

$$H_0: \mu_{\tau_w}^{(S)} - \mu_{\tau_w}^{(C)} = 0 \tag{4.1}$$

$$H_s: \mu_{\tau_w}^{(S)} - \mu_{\tau_w}^{(C)} > 0 \tag{4.2}$$

where $\mu_{\tau_w}^{(S)}$ is the inferred population mean WSS of the sutured anastomosis and $\mu_{\tau_w}^{(C)}$ is the inferred population mean WSS of the coupled anastomosis.

A Lillie test was carried out to ensure data was normally distributed, and subsequently a homoscedastic one-tailed *Gosset Student's* t-test was performed at the 99.9% confidence level on two convenient samples of data collected from the simulated anastomotic sites of each technique. As mentioned in 3.5, a one-tailed t-test was used as the raw data demonstrated a

change on one direction only (104). Incidentally, a two-tailed test also shows a statistically significant result. A summary of the t-test is shown in Table 4.1.

	Sample size	Mean WSS (Pa)	Variance
<i>Sutured</i>	18	8.38	2.07
<i>Coupled</i>	16	3.16	1.42
Summary			
<i>Degrees Of Freedom</i>	32	<i>Hypothesized Mean Difference</i>	0
<i>Test Statistics (t-value)</i>	11.43	<i>Pooled Variance</i>	1.76
<i>One-tailed distribution</i>			
<i>p-level</i>	3.83×10^{-13}	<i>t Critical Value (p 0.1%)</i>	3.36

Table 4.1 - Student's t-test of WSS for sutured and coupled simulations (p <0.1%)

5 Discussion

Although there have been many studies performed using CFD to evaluate flow within blood vessels, none of these have examined in detail the local fluid dynamics around sutured and coupled microvascular anastomoses. This study has utilised the commercial CFD code ANSYS CFX to specifically target the local fluid properties at suture sites and the coupler interface; thus investigating the potential for intravascular thrombus formation in these two techniques. The clinical implications of the modelling work are presented in this chapter together with pertinent statistical analysis of data pertaining to potential formation of intravascular thrombosis.

5.1 Clinical

This study has demonstrated that the flow patterns in sutured and coupled microvascular anastomoses vary sufficiently to produce different physical properties at the anastomotic site, and as such they have different potential effects on coagulation and thrombus formation. Purely based on the data gathered from the simulations performed, clot formation appears to be more likely using the sutured technique rather than the coupler.

Although the widely held opinion in the surgical community is that a coupled venous anastomosis is as good as a sutured anastomosis, there are studies demonstrating *reduced* thrombosis rates in comparative series (1.5% vs. 3.3% (21)) and very low thrombosis rates (0.6% (30)) for coupled venous anastomoses. These clinical studies provide good evidence in favour of the microvascular venous coupler.

Thrombus formation in hand sutured arterial anastomoses accounts for approximately 25% of all post operative vessel thromboses (107). This represents around 1% of all free flaps (107,108) and, whilst this is low, it signifies a large number of failed free flaps. As arterial

coupling is not routine practice, there is little data to evaluate for comparison with arterial sutured anastomoses. In addition, the studies that have been performed include relatively low numbers, around 50 – 100 (31–33), when compared with those carried out on venous coupled anastomoses, where 1000 anastomoses were evaluated (30). Consequently, the thrombosis rates in coupled anastomoses range from 0% (0/62) (33) to 3.2% (4/124) (32). It is therefore difficult to draw firm conclusions from the available clinical data as to the success of arterial coupling.

The present research has generated raw theoretical physical data supporting the clinical findings of these studies: that the coupled anastomosis is less likely to precipitate thrombus formation. Furthermore, solely on the physical findings noted, it is possible to recommend that, should a sutured anastomosis be performed, the smallest possible number of sutures should be placed in order to minimise their thrombogenic potential, whilst maintaining a well-sealed anastomosis.

In addition to the physical flow properties of the sutured anastomosis being more thrombogenic than that of the coupler; the time taken to perform a sutured anastomosis is far greater than the coupled technique, as described in section 2.1.1. Based on the combination of less favourable flow properties, and a longer operative time, the sutured method can be depicted as an inferior technique.

The potential impact of this research lies in the ability to transfer these findings into clinically relevant and applicable recommendations. Although the simulations in this project have been accurately created under reliable and realistic physical conditions, the models are idealised and rely on a series of assumptions which may not translate directly into clinical practice. These include vessels with non-compliant walls, and the steady-state nature of blood flow. Bearing this in mind, there are a number of recommendations for further work (section 6.2), which could be applied to this study to address these issues. Despite this, it is likely that the fundamental fluid flows resulting from geometrical differences in the anastomotic techniques

will remain largely unchanged. This implies that as long as there are sutures, or a coupler, at the anastomotic site, there will be geometrical changes in the lumen of the vessel that can propagate blood clots, irrespective of the increased accuracy of the boundary conditions (e.g. compliant walls, pulsatile flow and non-Newtonian fluid).

5.2 Analytical

The mean values in Table 4.1 indicate an overall greater mean WSS for the sutured anastomosis. As the variance of the samples is quite different it is not appropriate to infer this is true for the whole population from this analysis alone. However, the test statistic (t-value) is very high (11.4) in this case, i.e. much greater than the critical t-value calculated at the 0.1% confidence level of 3.36; which indicates a highly statistically significant result as evidenced by the probability of the null hypothesis ($p=3.83 \times 10^{-13}$). Incidentally the homoscedastic assumption was validated via an appropriate Fisher's F-test where the test's null hypothesis was retained at the 2% confidence level as shown below in Table 5.1.

	Coupled	Sutured		
<i>Sample size</i>	16	18		
<i>Mean WSS (Pa)</i>	3.16	8.38		
<i>Variance</i>	1.42	2.07		
<i>Standard Deviation</i>	1.19	1.43		
<i>Mean Standard Error</i>	0.29	0.33		
Summary				
<i>F</i>	1.44	<i>F Critical value (2%)</i>	2.96	
<i>p-level 1-tailed</i>	0.23			
<i>H0 (2%)?</i>	<i>accepted</i>			

Table 5.1 - F test (Fisher's) for WSS in sutured and coupled simulations ($p < 2\%$)

This implies overwhelming statistical evidence for rejection of the null hypothesis (4.1) in favour of the scientific hypothesis (4.2). Thereby inferring that the values of the WSS in the sutured anastomosis are indeed greater than those of the coupled anastomosis. Initiation of

thrombosis formation is therefore more likely in the sutured anastomotic technique as there is an increase of 28% in the average WSS when compared to the coupled method. Incidentally, the maximum WSS seen in the sutured model is approximately 1.5 times greater than that in the coupled, when using the pristine model as a benchmark.

Shear Strain Rates (SSR) were not analysed statistically as the SSR is directly proportional to WSS in Newtonian fluids. Hence, the statistical results would reveal the same relationship.

From a qualitative perspective, the vorticity profiles demonstrate that a greater proportion of the fluid directly at the sutured anastomosis site has a vorticity above that which would occur in a pristine vessel, when compared to the coupled anastomosis. In addition, these vortices appear to occur in greater concentrations around the sutures and are better dispersed in the coupled simulation. Although there is little evidence in the literature to verify the extent to which vorticity may impact on thrombus formation, it is known that disrupted flow can precipitate coagulation (14). As such, the proportion of the fluid forming vortices at the anastomotic site could be interpreted as disrupted flow and hence potentially thrombogenic.

5.3 Summary

During this study, a rigorous benchmarking process was followed where analytical and numerical Newtonian fluid models were produced. Good agreement was demonstrated between the analytical and numerical modelling calculations, implying the simulations presented throughout this thesis can be regarded as reacting in a physically realistic manner. Initially, models of pristine vessels were created which simulated blood flow in human microvessels. The models presented were shown to be reliable and accurate, and are analogous to those present in the current relevant literature e.g. (40,75,82).

The modelling strategy used steady-state analyses to examine the local fluid dynamics of both sutured and coupled microarterial anastomoses, which is a comparison (to the author's

knowledge) not previously made in either the clinical or scientific literature. Whilst the steady-state models are not physiologically representative, they form a reliable benchmark from which subsequent work can continue.

Data obtained from the sutured anastomosis simulation revealed reduced boundary velocities at the suture sites, and increased maximum (9.9 Pa) and average (4.5 Pa) WSS throughout the vessel. Both these parameters are implicated in the initiation of thrombosis. The most significant finding was an especially high WSS (9.9 Pa) observed at the suture sites themselves, with a SSR significantly greater than $1 \times 10^3 \text{ s}^{-1}$; the figure above which platelet activation, and subsequently thrombus formation, is expected (93,94).

The results from the coupled model show some reduction in boundary velocity at the anastomosis, and comparable maximum (4.8 Pa) and average (3.5 Pa) WSS to that of the pristine vessel (3.5 and 3.8 Pa, respectively). The velocity changes are similar to that of the sutured anastomosis. As such, it appears that WSS and SSR are most likely responsible for initiation of thrombosis formation, rather than purely changes in velocity profile.

The coupled anastomosis simulation shows a small increase in WSS in the anastomotic region compared to the pristine model. However, this is less than half that of the sutured model (4.8 Pa compared with 9.9 Pa respectively), with a SSR $\sim 1 \times 10^3 \text{ s}^{-1}$, at the borderline of thrombus initiation.

The vorticity profile for the coupled anastomosis demonstrates qualitatively that a higher proportion of the fluid has a vorticity greater than would be expected in a pristine vessel. However, the vorticity profile in the sutured anastomosis shows a larger amount of vorticity at the anastomotic site when compared to both the coupled and pristine vessels. This is a potential indicator for disrupted flow and hence thrombus formation. Importantly, it is recognised that the vorticity is a qualitative observation and is therefore not a dependable variable for analysis.

Whilst observations from the sutured simulation would individually suggest an increased chance of blood clot formation, taken together, they potentially demonstrate a more thrombogenic profile when compared to a pristine, or indeed a coupled vessel. Data from the coupled simulations reveal a profile that may be less thrombogenic than that of the sutured anastomosis, and that is almost equivalent to that of the pristine vessel.

6 Conclusions and recommendations

A range of conclusions can be made regarding the local flow properties through sutured and coupled anastomoses as a result of this research. These are detailed concisely below, and reflect achievement of the aim and objectives set at the beginning of the thesis (section 1.4). Importantly, as this study involves several assumptions being made about the fluid properties and boundary conditions, and is very much idealised, there are a range of recommendations for further work to permit more clinically and biologically realistic simulations to be performed.

Overall, the data show that null hypothesis can be rejected in favour of the research hypothesis.

6.1 Conclusions

With respect to the aim and objectives of the thesis, the following conclusions can be drawn.

- Good agreement was demonstrated between the analytical and numerical modelling calculations.
- The models presented in this thesis were shown to be reliable and accurate.
- Comparison of fluid dynamics through sutured and coupled anastomoses has not, to the author's knowledge, been previously made in either the clinical or scientific literature.
- A reduced boundary velocity was seen at suture sites, and an increased maximum and average WSS found throughout the vessel.
- An especially high WSS was observed at the suture sites themselves, with a SSR of significantly greater than that where platelet activation is expected.

- A reduction in boundary velocity, and comparable maximum and average WSS to that of the pristine vessel, was seen in the coupled simulation.
- The coupled anastomosis simulation shows a small increase in WSS in the anastomotic region compared to the pristine model.
- The vorticity profile in the sutured anastomosis shows quantitatively a larger amount of vorticity at the anastomotic site when compared to both the coupled and pristine vessels.

Overall, it can be concluded that, within the limits of CFD simulations and the assumptions taken in this study, a sutured anastomosis is potentially more likely to generate an intravascular thrombosis than a coupled anastomosis.

6.2 Recommendations for further work

This study has examined in detail the local flow patterns around sutured and coupled microvascular anastomoses in steady-state arterial models. All models in this research were, however, very much *idealised* and as such cannot directly represent the flow patterns that may be found in human vessels after microvascular surgery. In order to make the models more representative of genuine blood vessels *in vivo*, a number of additional features could be taken into consideration. These were outside the scope of the work presented in this thesis, but would make a range of topics suitable for further research in this field.

Potential avenues for further investigation are detailed below:

- Venous microvascular anastomosis simulations for comparison
- Pulsatile blood flow
- Vessel wall compliance
- Mechanical properties of sutures/coupler

- Curved and/or branching vessels
- Irregularly placed sutures and/or different sized suture material
- Non-Newtonian model to compare directly with the present Newtonian data
- Realistic geometries from image-based recreations of human vessels
- Design optimisation for a novel artery specific coupling device

References

1. Jassinowski A. Die Arteriennhat: Eine experimentelle Studie. Inaug Diss Dorpat. 1889; 1-103.
2. Carrel A. La technique operatoire des anastomoses vasculaires et la transplantation des visceres. Lyon med. 1902; 98: 859-864.
3. Jacobson JH II, Suarez EL. Microsurgery in anastomosis of small vessels. Surg Forum. 1960; 11:243–245.
4. Malt RA, Mckhann CF. Replantation of Severed Arms. The Journal of the American Medical Association. 1964; 189(10):716 –722.
5. Komatsu S, Tamai S. Successful Replantation of A Completely Cut-Off Thumb. Plast Reconstr Surg. 1968; 42(4):374–377.
6. McLean DH, Buncke HJ Jr. Autotransplant of omentum to a large scalp defect, with microsurgical revascularization. Plast Reconstr Surg. 1972; 49(3):268–274.
7. Daniel RK, Taylor GI. Distant transfer of an island flap by microvascular anastomoses: A clinical technique. Plast Reconstr Surg. 1973; 52(2):111–117.
8. O’Brien BM, MacLeod AM, Hayhurst JW, Morrison WA. Successful transfer of a large island flap from the groin to the foot by microvascular anastomoses. Plast Reconstr Surg. 1973; 52(3):271–278.
9. Petruzzo P, Testelin S, Kanitakis J, Badet L, Lengelé B, Girbon J-P, et al. First Human Face Transplantation: 5 Years Outcomes. Transplantation. 2012; 93(2):236–240.
10. Evans BCD, Evans GRD. Microvascular Surgery. Plast Reconstr Surg. 2007; 119(2):18e–30e.
11. Yap LH, Butler CE. Principles of Microsurgery. Grabb and Smith’s Plastic Surgery. 6th Revised edition. Pages 66–72: Lippincott Williams and Wilkins; 2006.
12. Curo. Breast reconstruction - patient information guide [Internet]. [cited 2011 Mar 26]. Available from: <http://www.bapras.org.uk/guide.asp?id=358>
13. Kroll SS, Schusterman MA, Reece GP, Miller MJ, Evans GR, Robb GL, et al. Choice of flap and incidence of free flap success. Plast Reconstr Surg. 1996; 98(3):459–463.
14. López JA, Chen J. Pathophysiology of venous thrombosis. Thrombosis Research. 2009; 123(Supplement 4):S30–S34.
15. White FM. Fluid Mechanics. 6th Edition., International Edition. Pages 3-48: McGraw-Hill Higher Education; 2009.
16. Fox RW, McDonald AT, Pritchard PJ. Introduction to Fluid Mechanics. 7th Edition. Pages 1-18: John Wiley & Sons; 2009.
17. Fox RW, McDonald AT, Pritchard PJ. Introduction to Fluid Mechanics. 7th Edition. Pages 19-44: John Wiley & Sons; 2009.

18. Newton I. *Philosophiæ Naturalis Principia Mathematica*. 1st Edition. Pages 1-40: London: S. PEPYS, Reg. Soc. PRÆSES.; 1686.
19. White FM. *Fluid Mechanics*. 6th ed., International Edition. Pages 341-423: McGraw-Hill Higher Education; 2009.
20. Ostrup LT, Berggren A. The UNILINK instrument system for fast and safe microvascular anastomosis. *Ann Plast Surg*. 1986; 17(6):521–525.
21. Yap LH, Constantinides J, Butler CE. Venous thrombosis in coupled versus sutured microvascular anastomoses. *Ann Plast Surg*. 2006; 57(6):666–669.
22. Zeebregts C, Acosta R, Bölander L, Van Schilfgaarde R, Jakobsson O. Clinical experience with non-penetrating vascular clips in free-flap reconstructions. *Br J Plast Surg*. 2002; 55(2):105–110.
23. Cope C. Technique and clinical experience of the Unilink/3M(R) microvascular anastomotic coupling device in free flap surgery. *Internet J Plast Surg*. 2001; 1(1).
24. Kirsch WM, Zhu YH, Hardesty RA, Chapolini R. A new method for microvascular anastomosis: report of experimental and clinical research. *Am Surg*. 1992; 58(12):722–727.
25. MacDonald JD. Learning to perform microvascular anastomosis. *Skull Base*. 2005; 15(3):229–240.
26. Nakayama K et al. A simple new method for small vessel anastomoses (free autograft of the sigmoid included). *Surgery*. 1962; 52:918–931.
27. Ostrup LT. Anastomosis of small veins with suture or Nakayama's apparatus. A comparative study. *Scand J Plast Reconstr Surg*. 1976; 10(1):9–17.
28. Hallock GG, Rice DC. Early experience with the new "megacoupler" ring-pins for microvascular anastomoses. *J Plast Reconstr Aesthet Surg*. 2008; 61(8):974–976.
29. Ahn CY, Shaw WW, Berns S, Markowitz BL. Clinical experience with the 3M microvascular coupling anastomotic device in 100 free-tissue transfers. *Plast Reconstr Surg*. 1994; 93(7):1481–1484.
30. Jandali S, Wu LC, Vega SJ, Kovach SJ, Serletti JM. 1000 consecutive venous anastomoses using the microvascular anastomotic coupler in breast reconstruction. *Plast Reconstr Surg*. 2010; 125(3):792–798.
31. Ross DA, Chow JY, Shin J, Restifo R, Joe JK, Sasaki CT, et al. Arterial coupling for microvascular free tissue transfer in head and neck reconstruction. *Arch Otolaryngol Head Neck Surg*. 2005; 131(10):891–895.
32. Chernichenko N, Ross DA, Shin J, Chow JY, Sasaki CT, Ariyan S. Arterial coupling for microvascular free tissue transfer. *Otolaryngol Head Neck Surg*. 2008; 138(5):614–618.
33. Spector JA, Draper LB, Levine JP, Ahn CY. Routine use of microvascular coupling device for arterial anastomosis in breast reconstruction. *Ann Plast Surg*. 2006; 56(4):365–368.
34. White FM. *Fluid Mechanics*. 6th Edition., International Edition. Pages 137-192: McGraw-Hill Higher Education; 2009.

35. White FM. Fluid Mechanics. 6th Edition., International Edition. Pages 225-273: McGraw-Hill Higher Education; 2009.
36. Einstein A. Die Grundlage der allgemeinen Relativitätstheorie. Annalen der Physik. 1916; 354(7):769–822.
37. Wendt JF, Anderson JD. Computational fluid dynamics: an introduction. Pages 3-15: Springer; 2009.
38. Blazek J. Computational Fluid Dynamics: Principles and Applications. Har/Cdr. Pages 1-26: Elsevier Science Ltd; 2001.
39. Weisstein EW. Cylindrical Coordinates -- from Wolfram MathWorld [Internet]. [cited 2012 Sep 20]. Available from: <http://mathworld.wolfram.com/CylindricalCoordinates.html>
40. Rickard RF, Meyer C, Hudson DA. Computational modeling of microarterial anastomoses with size discrepancy (small-to-large). J Surg Res. 2009; 153(1):1–11.
41. Wendt JF, Anderson JD. Computational fluid dynamics: an introduction. Pages 15-51: Springer; 2009.
42. Friedman MH, Hutchins GM, Barger CB, Deters OJ, Mark FF. Correlation between intimal thickness and fluid shear in human arteries. Atherosclerosis. 1981; 39(3):425–436.
43. Xu XY, Collins MW. A review of the numerical analysis of blood flow in arterial bifurcations. Proc Inst Mech Eng H. 1990; 204(4):205–216.
44. Kleinstreuer C, Hyun S, Buchanan JR, Longest PW, Archie JP, Truskey GA. Hemodynamic parameters and early intimal thickening in branching blood vessels. Crit Rev Biomed Eng. 2001; 29(1):1–64.
45. Perktold K, Florian H, Hilbert D. Analysis of pulsatile blood flow: a carotid siphon model. J Biomed Eng. 1987; 9(1):46–53.
46. Perktold K, Peter R. Numerical 3D-stimulation of pulsatile wall shear stress in an arterial T-bifurcation model. J Biomed Eng. 1990; 12(1):2–12.
47. Perktold K, Nerem RM, Peter RO. A numerical calculation of flow in a curved tube model of the left main coronary artery. J Biomech. 1991; 24(3-4):175–189.
48. Perktold K, Resch M, Peter RO. Three-dimensional numerical analysis of pulsatile flow and wall shear stress in the carotid artery bifurcation. J Biomech. 1991; 24(6):409–420.
49. Ku DN, Giddens DP, Zarins CK, Glagov S. Pulsatile flow and atherosclerosis in the human carotid bifurcation. Positive correlation between plaque location and low oscillating shear stress. Arteriosclerosis. 1985; 5(3):293–302.
50. Hughes PE, How TV. Flow structures at the proximal side-to-end anastomosis: Influence of geometry and flow division. J Biomech Eng. 1995; 117(2):224–236.
51. Ojha M. Wall shear stress temporal gradient and anastomotic intimal hyperplasia. Circ Res. 1994 ;74(6):1227–1231.

52. Hofer M, Rappitsch G, Perktold K, Trubel W, Schima H. Numerical study of wall mechanics and fluid dynamics in end-to-side anastomoses and correlation to intimal hyperplasia. *J Biomech.* 1996; 29(10):1297–1308.
53. DePaola N, Gimbrone MA Jr, Davies PF, Dewey CF Jr. Vascular endothelium responds to fluid shear stress gradients. *Arterioscler Thromb.* 1992; 12(11):1254–1257.
54. Bryant SR, Bjercke RJ, Erichsen DA, Rege A, Lindner V. Vascular remodeling in response to altered blood flow is mediated by fibroblast growth factor-2. *Circ Res.* 1999; 84(3):323–328.
55. Hoskins PR. Quantitative techniques in arterial Doppler ultrasound. *Clin Phys Physiol Meas.* 1990; 11 Suppl A:75–80.
56. Pelc NJ, Herfkens RJ, Shimakawa A, Enzmann DR. Phase contrast cine magnetic resonance imaging. *Magn Reson Q.* 1991; 7(4):229–254.
57. Smedby O. Angiographic methods for the study of fluid mechanical factors in atherogenesis. *Acta Radiol Suppl.* 1992; 380:1–38.
58. Steinman DA. Image-based computational fluid dynamics modeling in realistic arterial geometries. *Ann Biomed Eng.* 2002; 30(4):483–497.
59. Leuprecht A, Perktold K, Kozerke S, Boesiger P. Combined CFD and MRI study of blood flow in a human ascending aorta model. *Biorheology.* 2002; 39(3-4):425–429.
60. Antiga L, Piccinelli M, Botti L, Ene-Iordache B, Remuzzi A, Steinman DA. An image-based modeling framework for patient-specific computational hemodynamics. *Med Biol Eng Comput.* 2008; 46(11):1097–1112.
61. Steinman DA, Taylor CA. Flow imaging and computing: large artery hemodynamics. *Ann Biomed Eng.* 2005; 33(12):1704–1709.
62. Taylor CA, Steinman DA. Image-based modeling of blood flow and vessel wall dynamics: applications, methods and future directions: Sixth International Bio-Fluid Mechanics Symposium and Workshop, March 28-30, 2008 Pasadena, California. *Ann Biomed Eng.* 2010; 38(3):1188–1203.
63. Karmonik C, Bismuth J, Davies MG, Lumsden AB. Computational fluid dynamics as a tool for visualizing hemodynamic flow patterns. *Methodist DeBakey Cardiovasc J.* 2009; 5(3):26–33.
64. Migliavacca F, Dubini G. Computational modeling of vascular anastomoses. *Biomech Model Mechanobiol.* 2005; 3(4):235–250.
65. Pietrabissa R, Inzoli F, Fumero R. Simulation study of the fluid dynamics of aorto-coronary bypass. *J Biomed Eng.* 1990; 12(5):419–424.
66. Steinman DA, Vinh B, Ethier CR, Ojha M, Cobbold RS, Johnston KW. A numerical simulation of flow in a two-dimensional end-to-side anastomosis model. *J Biomech Eng.* 1993; 115(1):112–118.
67. Bertolotti C, Deplano V, Fuseri J, Dupouy P. Numerical and experimental models of post-operative realistic flows in stenosed coronary bypasses. *J Biomech.* 2001; 34(8):1049–1064.

68. Papaharilaou Y, Doorly DJ, Sherwin SJ, Peiro J, Griffith C, Cheshire N, et al. Combined MR imaging and numerical simulation of flow in realistic arterial bypass graft models. *Biorheology*. 2002; 39(3-4):525–531.
69. Ballyk PD, Steinman DA, Ethier CR. Simulation of non-Newtonian blood flow in an end-to-side anastomosis. *Biorheology*. 1994; 31(5):565–586.
70. Lei M, Kleinstreuer C, Archie JP. Geometric design improvements for femoral graft-artery junctions mitigating restenosis. *J Biomech*. 1996; 29(12):1605–1614.
71. Lei M, Kleinstreuer C, Archie JP. Hemodynamic simulations and computer-aided designs of graft-artery junctions. *J Biomech Eng*. 1997; 119(3):343–348.
72. Lei M, Archie JP, Kleinstreuer C. Computational design of a bypass graft that minimizes wall shear stress gradients in the region of the distal anastomosis. *J Vasc Surg*. 1997; 25(4):637–646.
73. Perktold K, Leuprecht A, Prosi M, Berk T, Czerny M, Trubel W, et al. Fluid dynamics, wall mechanics, and oxygen transfer in peripheral bypass anastomoses. *Ann Biomed Eng*. 2002; 30(4):447–460.
74. Al-Sukhun J, Lindqvist C, Ashammakhi N, Penttilä H. Microvascular stress analysis. Part I: simulation of microvascular anastomoses using finite element analysis. *Br J Oral Maxillofac Surg*. 2007; 45(2):130–137.
75. Berti G. @neurIST D23v2 - Analysis Protocols Version 2 [Internet]. 2010 [cited 2012 Apr 20]. Available from: http://www.aneurist.org/UserFiles/File/PUBLIC_DELIVERABLES/D23v2_v1.2_final.pdf
76. Chaniotis AK, Kaiktsis L, Katritsis D, Efstathopoulos E, Pantos I, Marmarellis V. Computational study of pulsatile blood flow in prototype vessel geometries of coronary segments. *Phys Med*. 2010; 26(3):140–156.
77. ANSYS Fluent Flow Modeling Simulation Software [Internet]. [cited 2012 Jun 21]. Available from: <http://www.ansys.com/Products/Simulation+Technology/Fluid+Dynamics/ANSYS+Fluent>
78. ANSYS CFX - CFD Software for Fluid Flow Modeling [Internet]. [cited 2012 Jun 21]. Available from: <http://www.ansys.com/Products/Simulation+Technology/Fluid+Dynamics/ANSYS+CFX>
79. Argonne Transportation Research and Analysis Computing Center :: Computing Resources :: STAR CD [Internet]. [cited 2012 Jun 21]. Available from: http://web.anl.gov/TRACC/Computing_Resources/star-cd.html
80. vmtk - the Vascular Modeling Toolkit [Internet]. [cited 2012 Jun 21]. Available from: <http://www.vmtk.org/Main/Overview/>
81. Abaqus/CFD - Dassault Systèmes [Internet]. [cited 2012 Jun 21]. Available from: <http://www.3ds.com/products/simulia/portfolio/abaqus/abaqus-portfolio/abaquscfd/>
82. Meyer C, Hudson D, Rickard R. Anastomotic Size Mismatch—Modeling of the Hemodynamics of Idealized Constructs by Means of Computational Fluid Dynamics. *J Reconstr Microsurg*. 2006; 22(04):A018.

83. Duck FA. Physical properties of tissue: a comprehensive reference book. Pages 137-167: Academic Press; 1990.
84. Vimmr J, Jonášová A. Non-Newtonian effects of blood flow in complete coronary and femoral bypasses. *Mathematics and Computers in Simulation*. 2010; 80(6):1324–1336.
85. Soulis JV, Giannoglou GD, Chatzizisis YS, Seralidou KV, Parcharidis GE, Louridas GE. Non-Newtonian models for molecular viscosity and wall shear stress in a 3D reconstructed human left coronary artery. *Med Eng Phys*. 2008; 30(1):9–19.
86. Chen J, Lu X-Y. Numerical investigation of the non-Newtonian pulsatile blood flow in a bifurcation model with a non-planar branch. *J Biomech*. 2006; 39(5):818–832.
87. Sakariassen KS, Nievelstein PF, Coller BS, Sixma JJ. The role of platelet membrane glycoproteins Ib and IIb-IIIa in platelet adherence to human artery subendothelium. *Br J Haematol*. 1986; 63(4):681–691.
88. Ismagilov RF, Stroock AD, Kenis PJA, Whitesides G, Stone HA. Experimental and theoretical scaling laws for transverse diffusive broadening in two-phase laminar flows in microchannels. *Applied Physics Letters*. 2000; 76(17):2376–2378.
89. Shaaban AM, Duerinckx AJ. Wall shear stress and early atherosclerosis: a review. *Am J Roentgenol*. 2000; 174(6):1657–1665.
90. Caro CG, Cheshire NJ, Watkins N. Preliminary comparative study of small amplitude helical and conventional ePTFE arteriovenous shunts in pigs. *J R Soc Interface*. 2005; 2(3):261–266.
91. Lowe GDO. Virchow's triad revisited: abnormal flow. *Pathophysiol Haemost Thromb*. 2003; 33(5-6):455–457.
92. Hathcock JJ. Flow effects on coagulation and thrombosis. *Arterioscler Thromb Vasc Biol*. 2006; 26(8):1729–1737.
93. Shen F, Kastrup CJ, Liu Y, Ismagilov RF. Threshold response of initiation of blood coagulation by tissue factor in patterned microfluidic capillaries is controlled by shear rate. *Arterioscler Thromb Vasc Biol*. 2008; 28(11):2035–2041.
94. Roth GJ. Developing relationships: arterial platelet adhesion, glycoprotein Ib, and leucine-rich glycoproteins. *Blood*. 1991; 77(1):5–19.
95. Weiss HJ, Turitto VT, Baumgartner HR. Role of shear rate and platelets in promoting fibrin formation on rabbit subendothelium: Studies utilizing patients with quantitative and qualitative platelet defects. *J Clin Invest*. 1986; 78(4):1072–1082.
96. Grabowski EF. Platelet aggregation in flowing blood at a site of injury to an endothelial cell monolayer: quantitation and real-time imaging with the TAB monoclonal antibody. *Blood*. 1990; 75(2):390–398.
97. Synovis Micro | Products | GEM Microvascular Anastomotic COUPLER | Features & Benefits [Internet]. [cited 2013 Feb 10]. Available from: http://www.synovismicro.com/gem_microvascular_anastomotic_coupler_features_and_benefits.php

98. Bark DL Jr, Para AN, Ku DN. Correlation of thrombosis growth rate to pathological wall shear rate during platelet accumulation. *Biotechnology and bioengineering* [Internet]. 2012 Apr 26 [cited 2012 Jul 14]; Available from: <http://www.ncbi.nlm.nih.gov/pubmed/22539078>
99. Chandran KB, Gao D, Han G, Baraniewski H, Corson JD. Finite-element analysis of arterial anastomoses with vein, Dacron and PTFE grafts. *Med Biol Eng Comput*. 1992; 30(4):413–418.
100. 14.3.2. Measures of Mesh Quality [Internet]. [cited 2012 Sep 20]. Available from: https://www.sharcnet.ca/Software/Fluent13/help/cfx_mod/i1323480.html
101. White FM. *Viscous Fluid Flow*. 3rd Revised edition. Pages 1-42: McGraw-Hill Higher Education; 2005.
102. Oyre S, Ringgaard S, Kozerke S, Paaske WP, Erlandsen M, Boesiger P, et al. Accurate noninvasive quantitation of blood flow, cross-sectional lumen vessel area and wall shear stress by three-dimensional paraboloid modeling of magnetic resonance imaging velocity data. *J Am Coll Cardiol*. 1998; 32(1):128–134.
103. ANSYS CFD-Post - Fluid Dynamics Post-Processor for Visualization [Internet]. [cited 2012 Jun 29]. Available from: <http://www.ansys.com/Products/Simulation+Technology/Fluid+Dynamics/ANSYS+CFD-Post>
104. Student. New tables for testing the significance of observations. *Metron*. 1925; 5:105–108.
105. Saint-Venant AJCB. Memoire sur la Torsion des Prismes. *Mem Divers Savants*. 1855; 14:233–560.
106. Murray CD. The Physiological Principle of Minimum Work: I. The Vascular System and the Cost of Blood Volume. *Proc Natl Acad Sci. U.S.A.* 1926; 12(3):207–214.
107. Bui DT, Cordeiro PG, Hu Q-Y, Disa JJ, Pusic A, Mehrara BJ. Free flap reexploration: indications, treatment, and outcomes in 1193 free flaps. *Plast Reconstr Surg*. 2007; 119(7):2092–2100.
108. Mao C, Yu G, Peng X, Guo C, Huang M. Postoperative vessel thrombosis and its management after free flap transfers in head and neck region. *Zhonghua Er Bi Yan Hou Tou Jing Wai Ke Za Zhi*. 2005; 40(6):415–418.

Presentations and publications

Wain RAJ, Whitty JPM, Dalal MD, Holmes MC, Ahmed W. Computational modelling of blood flow through sutured and coupled microvascular anastomoses (Poster presented at the Regional Rosemere Cancer Foundation Annual Open Day, Preston, October 2012)

Wain RAJ, Whitty JPM, Dalal MD, Holmes MC, Ahmed W. Microvascular anastomoses using sutures and couplers: a computational study of blood flow characteristics (Abstract accepted by BAPRAS for the Summer Scientific Meeting, June 2013 for podium presentation)